Numerical Modelling of the Oldroyd-B Fluid

by

Nkosilathi Vundla

Thesis Presented for the Degree of
Master of Science in Engineering in Mechanical Engineering
University of Cape Town
November 2018

Declaration

I know the meaning of plagiarism and declare that all the work in the document, save for that which is properly acknowledged, is my own. This thesis/dissertation has been submitted to the Turnitin module (or equivalent similarity and originality checking software) and I confirm that my supervisor has seen my report and any concerns revealed by such have been resolved with my supervisor.

Signature: Signed by candidate

Abstract

The purpose of this thesis is to develop a 3D finite element model of the Oldroyd-B fluid for use in a complex geometry. The model is developed in deal.ii, which is a C++ finite element library. In addition to the standard finite element approach for the momentum equation, the discontinuous Galerkin method is used for the constitutive relation of the fluid model, with the extra stress as the unknown variable.

The model developed is verified by using the symmetric "flow over a cylinder" benchmark problem. The effect of using piecewise-constant discontinuous and bilinear discontinuous elements for the extra stress field is investigated. The the results of the scheme are compared to those found in literature.

The model is implemented in the solution of a complex problem of blood flow in an arteriovenous fistula, using geometry acquired from MRI data. A resistance boundary condition is used for the outlets. The flow profiles obtained from using both the Newtonian and Oldroyd-B fluids are validated against velocity encoded MRI and also compared to Fluid-Structure Interaction results for Newtonian fluids, from the literature. The effect of using a viscoelastic fluid on the flow profile and wall shear stresses are investigated.

The results from this work show that using a viscoelastic fluid, rather than a Newtonian fluid, provides additional details regarding the wall shear stress in the arteriovenous fistula.

Acknowledgements

I would like to express my gratitude to my supervisor Prof. B.D. Reddy for providing this opportunity and his support and willingness to share his experience. No matter how hard it seemed, Prof was always patient and ready to provide guidance.

I would also like to thank my colleagues from CERECAM for their support and companionship during this project. I would especially like to thank Dr Andie De Villiers for her invaluable advise regarding deal.ii, Winston Guess for always encouraging me, Dr Michael Malahe for his willingness always to lend an ear for my ideas and Maien Hamed for his technical help. I would like to name a few CERECAM members who helped provide a friendly environment, Emma Griffiths, Ritesh Rama, Mehdi Shizardi, Helen Liedke and Heidi Burger.

I would like to thank my family and friends for their continued support during this journey, especially my mother who always believed in me no matter how low I fell and my sister who was willing to shoulder my burden towards the end of the journey.

This project was financially supported by the South African Research Chair in Computational Mechanics.

Contents

List of Tables

List of Figures

Nomenclature

FSI	Fluid-Structure Interaction
MRI	Magnetic resonance imaging
PTT	Phan-Thien-Tanner
FENE	Finite Extendible Nonlinear Elasticity
HWNP	High Weissenburg number problem
DG	Discontinuous Galerkin
DEVSS	Discrete Elastic Viscous Stress Splitting
GLS	Galerkin Least Squares
UCM	Upper convected Maxwell
EVSS	Elastic Viscous Stress Splitting
MXI	A Galerkin/least-square fomulation, formed by the mass-continuity residual.
SUPG	Streamline Upwind Petrov Galerkin
DAVSS	discrete adaptive elastic viscous split stress
SMART	Sharp and Monotonic Algorithm for Realistic Transport
SPH	smoothed particle hydrodynamincs
LUST	locally up-winded spectral technique
AVF	arteriovenous Fistula
CFD	Computational fluid dynamics

Chapter 1

Introduction

1.1 Background

Fluid flow modelling has been applied in various areas of engineering such as the aerospace, chemical, biomedical and automotive industries, as a part of the design process. Traditionally modelling has been confined to the use of Newtonian fluids, which are the simplest of viscous fluids. Real fluids however, generally behave in a more complex manner. The approach then becomes the coupling of the mathematical models of the fluid to the equation of motion. For incompressible Newtonian fluids this leads to the Navier-Stokes equation.

Figure 1.1: Viscoelastic behaviour (a) rod climbing (*https://nnf.mit.edu/home/billboard/topic-5*) and (b) die swelling (*https://science.wonderhowto.com/how-to/perform-barus-effect-247644/*).

Viscoelastic fluids are an example of complex fluids; these exhibit both viscous and elastic behaviour. Examples of viscoelastic fluids are polymer solutions and blood. Various models have been developed in order to simulate viscoelastic behaviour; examples include the Upper Convected Maxwell, Oldroyd-B, Phan-Thien-Tanner (PTT), Finite Extendible Nonlinear Elasticity (FENE) and the Giesekus model.

The objective of this work is to develop a 3D computational model of the Oldroyd-B fluid, and to use this model to simulate blood flow in a realistic setting. The Oldroyd-B

fluid has been used in a wide range of applications such as heating, blood flow and flow through porous media [4]. A generalised Oldroyd-B model was also used in [5] to model blood, and was validated experimentally using porcine blood. Emphasis has been placed on shear thinning, using the Generalized Oldroyd-B fluid, in [6].

Studies on the Oldroyd-B fluid have also been focused on the high Weissenburg number problem (HWNP). The HWNP is the term that is used to refer to a common problem encountered when modelling the Oldroyd-B fluid, were all methods fail to converge with increasing Weissenburg numbers [7] (a dimensionless number in the Oldroyd B equation). This work will not focus on the HWNP, but its effects will still need to be taken into account in developing and implementing the algorithms in this work.

In this work a constant viscosity Oldroyd-B fluid will be used to keep the complexity of the problem within the scope of this work. The numerical method of choice for modelling the Oldroyd-B fluid is the finite element method, with discontinuous Galerkin methods being used to discretise the constitutive relation. The discontinuous Galerkin method is an alternative discretisation method in which the discrete solutions are discontinuous across element boundaries. The DG method is used to ensure a stable solution as the conforming Galerkin discretisation is sometimes unstable when handling advection reaction equations such as the constitutive relation for the Oldroyd-B fluid. DG methods have been used for the Oldroyd-B fluid [6, 8]. Alternatives to using DG methods in literature include Discrete Elastic Viscous Stress Splitting (DEVSS) [9], Local Projection Stabilization [10], the Galerkin Least Squares (GLS) [11], and the extended finite element method (XFEM) [12].

1.2 Aim and Objectives

The aim of this work is to develop a 3D finite element model of the Oldroyd-B fluid. The DG method will be used for the constitutive relation. The finite element model will be developed in deal.ii, which is an open source C++ finite element library. The model will be verified using benchmark problems and compared to solutions in the literature.

The goal is to use the model in a complex flow scenario viz, blood flow in an arteriovenous fistula as this model includes a complex geometry and features flow recirculation [3, 13]. A 3D finite element model using a Newtonian fluid will be validated by comparing the results to MRI data and fluid structure interaction simulations performed in [3]. The simulations in [3] were carried out for a Newtonian fluid. Results using the Oldroyd-B fluid will then be compared to to those obtained using a Newtonian fluid.

The effect of using a viscoelastic fluid on the flow profile and wall shear stresses will be analysed, with the view to determine the influence of adopting a complex viscoelastic model in such simulations.

1.3 Outline

The structure of the rest of this work is as follows. Chapter 2 introduces the governing equations for the Oldroyd-B fluid. The continuum theory required to derive the equations of motion for fluids is described. The extension from a Newtonian model to the Oldroyd-B fluid is outlined. Additionally, generalized forms of fluid models and alternative viscoelastic models are also discussed.

Chapter 3 presents the methods used to solve the Oldroyd-B system of partial differential equations. The weak form and the numerical approximation of solutions to systems of equations are introduced. Galerkin approximations are described along with the finite element method, and the elements used for the continuous Galerkin methods. The details of the discontinuous Galerkin method are given, including the introduction of discontinuous elements. The chapter concludes with the discontinuous Galerkin approximation of the Oldroyd-B equations from chapter 2.

Chapter 4 addresses the linearisation of non-linear equations and the implementation of the model. The modified Newton-Raphson method is introduced and used to linearise the Oldroyd-B fluid. The brief overview of the is implementation of the model in deal.ii is given, with outlines of some of the algorithms involved. Adaptive mesh refinement methods used are also discussed in the context of deal.ii, introducing the concept of hanging nodes. The chapter ends with a section on parallel computing methods used in the implementation.

The model used is verified in Chapter 5. An overview of the history of the flow past a cylinder benchmark problem is given. The benchmark is described and the parameter used in the problem are included. The solution profiles obtained are shown, and results of a mesh convergence study presented. An analysis of the benchmark using various measures of accuracy from the results follows. The effect of using different elements for the extra stress field in the model is also analysed.

Chapter 6 is concerned with the application of the model to a complex blood flow scenario. The chapter begins with a brief description of the mechanical properties of blood. A description of the arteriovenous fistula is given followed by a brief history of other work

carried out in this context. Additional considerations required for the boundary conditions of the model in the context of blood flow in complex geometries are discussed. The flow profile and wall shear stress results obtained for blood flow using a Newtonian fluid are shown. A comparison of the results obtained for a Newtonian fluid and the Oldroyd-B fluid is given. The chapter concludes with the analysis of the effect of using a viscoelastic fluid on the flow profile and wall shear stresses.

The final chapter discusses the conclusions of this work and potential future work based on this work.

Chapter 2

Governing Equations

This chapter outlines the governing equations for the Oldroyd-B fluid. The chapter begins with the kinematics of a continuous medium and its deformation. The conservation of mass and momentum are then used to derive equations that govern the behaviour of all media. A more comprehensive description on continuum mechanics can be found in [14].

Constitutive relations describing specific types of fluids and their responses are then derived. In this section the concept of Newtonian and Non-Newtonian fluids are introduced. Theory on Generalised Newtonian Fluids is addressed next. The last section of this chapter looks at different viscoelastic models. This section begins with linear viscoelastic theory and ends with corotational theory on which more complex models are based. The corotational theory leads to the Oldroyd 8-constant model from which the Oldroyd-B model is obtained. The chapter then reviews other useful viscoelastic models. Material on derivations of various fluid models and their applications can be found in [15, 16].

2.1 Kinematics of Deformable Bodies

We consider a body $\mathcal{B}$ occupying a region Ω_0 at reference time t_0. The body consists of material points (particles) identified by their positions in the region ($\boldsymbol{X}$) at the reference time, i.e. the reference configuration. The motion of a material point from the reference configuration to the current configuration at time $t = t'$ is given by the invertible map

$$\boldsymbol{x} = \boldsymbol{\varphi}(\boldsymbol{X}, t). \tag{2.1}$$

The motion of the body $\mathcal{B}$ is illustrated in Figure 2.1.

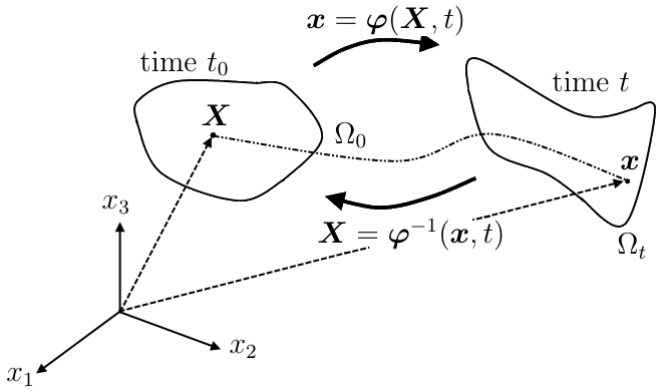

Figure 2.1: Motion of a material point in body $\mathcal{B}$

Quantities (such as velocity, temperature and stress) of a continuum in motion can be expressed in terms of either the reference configuration or the current configuration. When quantities are expressed in terms of the reference configuration, this is called the Lagrangian (material) description. Expressing quantities in terms of the current configuration on the other hand is known as the Eulerian (spatial) description. In the Eulerian framework changes are observed at fixed locations in space. The Eulerian framework is generally used in fluid mechanics. Quantities can be changed between material and spatial because of the assumed invertibility of $\boldsymbol{\varphi}$.

The velocity of a material point in the body is given in the material description by

$$\boldsymbol{u}(\boldsymbol{X}, t) = \frac{\partial \boldsymbol{\varphi}(\boldsymbol{X}, t)}{\partial t}.$$

The acceleration of a material point is given by the material derivative of its velocity; given a material description of the velocity $\boldsymbol{u}(\boldsymbol{X}, t)$, the acceleration is

$$\boldsymbol{a} = \frac{d^2\boldsymbol{\varphi}}{dt^2} = \frac{\partial \boldsymbol{u}(\boldsymbol{X}, t)}{\partial t}.$$

When given the spatial description of the velocity $\boldsymbol{u}(\boldsymbol{x}, t)$, the chain rule is used to obtain the acceleration as the material derivative of the velocity; that is,

$$\begin{aligned} \frac{Du_i}{Dt} &= \frac{\partial u_i}{\partial t} + \frac{\partial u_i}{\partial x_j}\frac{\partial x_j}{\partial t} \\ \text{or } \frac{D\boldsymbol{u}}{Dt} &= \frac{\partial \boldsymbol{u}}{\partial t} + (\nabla \boldsymbol{u})\boldsymbol{u}. \end{aligned} \tag{2.2}$$

The velocity gradient $\nabla \boldsymbol{u}$ can be decomposed into its symmetric and antisymmetric parts.

The symmetric part $\bar{\boldsymbol{D}}$ is the rate of deformation tensor given by

$$\bar{\boldsymbol{D}} = \frac{1}{2}(\boldsymbol{\nabla u} + (\boldsymbol{\nabla u})^T).$$

The antisymmetric part $\boldsymbol{W}$ is the spin tensor, given by

$$\boldsymbol{W} = \frac{1}{2}(\boldsymbol{\nabla u} - (\boldsymbol{\nabla u})^T). \tag{2.3}$$

Another important kinematic property related to the velocity gradient $\nabla \boldsymbol{u}$, is the vorticity

$$\boldsymbol{\omega} = \nabla \times \boldsymbol{u}. \tag{2.4}$$

The vorticity describes rotational motion.

2.2 Balance Laws

2.2.1 Balance of Mass

Consider an arbitrary volume $V(t)$ in the domain Ω. The principle of conservation of mass states that

$$\frac{Dm}{Dt} = \frac{D}{Dt}\int_{V(t)} \rho \, \mathrm{d}V = 0.$$

Here m is the mass of $V(t)$ and ρ the density. For a field $f(\boldsymbol{x}, t)$, the Reynolds Transport theorem is as follows:

$$\frac{D}{Dt}\int_{V(t)} f \, \mathrm{d}V = \int_{V(t)} \left(\frac{\partial f}{\partial t} + \nabla \cdot (f\boldsymbol{u})\right) \, \mathrm{d}V.$$

Applying the Reynolds transport theorem to the mass conservation equation yields

$$\int_{V(t)} \left(\frac{\partial \rho}{\partial t} + \nabla \cdot (\rho \boldsymbol{u})\right) \, \mathrm{d}V = 0. \tag{2.5}$$

Given that $V(t)$ is arbitrary the integrand must be equal to zero, which yields the continuity equation,

$$\frac{\partial \rho}{\partial t} + \nabla \cdot (\rho \boldsymbol{u}) = 0. \tag{2.6}$$

For a fluid with constant density, equation (2.6) simplifies to the incompressibility constraint

$$\nabla \cdot \boldsymbol{u} = 0. \tag{2.7}$$

2.2.2 Balance of Linear and Angular Momentum

The balance of linear momentum states that the rate of change of momentum of an arbitrary volume $V(t)$ is equal to the total forces acting on that volume. That is,

$$\frac{D}{Dt} \int_{V(t)} \rho \boldsymbol{u} \, \mathrm{d}V = \int_{V(t)} \boldsymbol{b} \, \mathrm{d}V + \int_{S(t)} \boldsymbol{t} \, \mathrm{d}S. \tag{2.8}$$

Here $\boldsymbol{b}$ represents the body force acting in the body and $\boldsymbol{t}$ represents the traction forces acting on the surface $S(t)$ of the volume $V(t)$. The surface traction is given by

$$\boldsymbol{t} = \boldsymbol{\sigma} \boldsymbol{n},$$

where $\boldsymbol{\sigma}$ is the Cauchy stress tensor and $\boldsymbol{n}$ is the outward facing normal. Thus equation (2.8) becomes

$$\frac{D}{Dt} \int_{V(t)} \rho \boldsymbol{u} \, \mathrm{d}V = \int_{V(t)} \boldsymbol{b} \, \mathrm{d}V + \int_{S(t)} \boldsymbol{\sigma} \boldsymbol{n} \, \mathrm{d}S.$$

The left hand side is then changed by Reynolds transport theorem and the surface integral is transformed to a volume integral by the divergence theorem to give

$$\int_{V(t)} \left(\frac{\partial \rho}{\partial t} + \nabla \cdot (\rho \boldsymbol{u}) - \boldsymbol{b} - \nabla \cdot \boldsymbol{\sigma} \, \mathrm{d}V \right) = 0.$$

Since $V(t)$ is an arbitrary volume, the integrand is zero; this gives Cauchy's equation of motion

$$\rho \frac{D\boldsymbol{u}}{Dt} - \nabla \cdot \boldsymbol{\sigma} = \boldsymbol{b}. \tag{2.9}$$

Balance of angular momentum can be used to show that the Cauchy stress $\boldsymbol{\sigma}$ tensor is symmetric; more detail can be found in §4.4 of [14]. Conservation of energy can be used to derive the internal energy equation which relates temperature to motion; however this work only considers isothermal flow problems so these derivations are omitted.

2.3 Newtonian Fluid

A constitutive relation is required to relate the stress tensor to the flow field $\boldsymbol{u}$. This effectively introduces a mathematical model for fluid properties to the balance equations derived in the previous section §2.2.

The simplest models that account for viscosity are referred to as Newtonian fluids. Fluids such as water and air can be assumed to be Newtonian fluids in standard conditions. The stress tensor for Newtonian fluids is linearly related to the rate of deformation tensor by the following equation:

$$\mathbf{T} = \eta \boldsymbol{D}, \tag{2.10}$$

where η is the fluid viscosity. In equation (2.10) the definition of $\boldsymbol{D}$ is redefined as twice that in equation (2.3). When incompressibilty is assumed, the stress $\boldsymbol{\sigma}$ is determined up to a pressure p. Hence we get

$$\boldsymbol{\sigma} = -p\boldsymbol{I} + \mathbf{T}. \tag{2.11}$$

In (2.11) the stress $\boldsymbol{\sigma}$ is split into a hydrostatic component dependent on pressure p and a part T which is a function of deformation. Substitution of the constitutive relation into equation (2.9) yields the Navier-Stokes equations for an incompressible isothermal fluid:

$$\rho \left(\frac{\partial \boldsymbol{u}}{\partial t} + \boldsymbol{u} \cdot \boldsymbol{\nabla} \boldsymbol{u} \right) + \boldsymbol{\nabla} p - \eta \boldsymbol{\nabla}^2 \boldsymbol{u} = \boldsymbol{b}, \tag{2.12}$$

$$\boldsymbol{\nabla} \cdot \boldsymbol{u} = \mathbf{0}. \tag{2.13}$$

2.4 Generalised Newtonian Fluid

Newtonian fluid models do not capture shear-rate dependent behaviour such as shear-thinning and shear-thickening seen in fluids such as tomato sauce, corn syrup, and blood. In order to capture this behaviour a class of fluids known as Generalised Newtonian fluids have been developed. In Generalised Newtonian fluid models the viscosity η of the fluid is a function of the invariants of the rate of deformation tensor $\boldsymbol{D}$.

The relation between the stress tensor and velocity gradient is no longer linear and takes the form

$$\mathbf{T} = \eta(\dot{\gamma})\boldsymbol{D},$$

where $\dot{\gamma}$ is the strain-rate, defined as the magnitude of the strain rate tensor; that is,

$$\dot{\gamma} = \sqrt{\tfrac{1}{2}\boldsymbol{D} : \boldsymbol{D}}.$$

The most basic type of Generalised Newtonian fluid model is the power law fluid for which the viscosity is proportional to an exponent of strain-rate: that is,

$$\mathbf{T} = k\dot{\gamma}^n\boldsymbol{D},$$

where k is a constant.

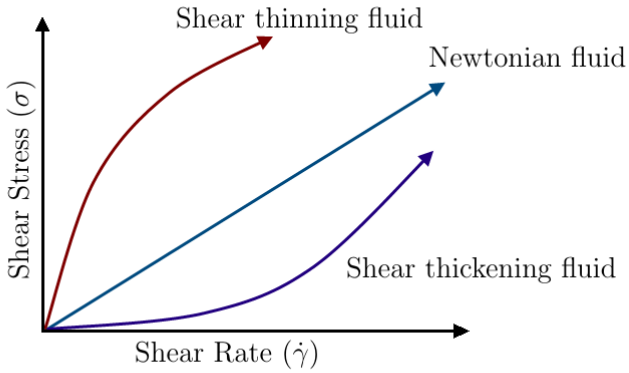

Figure 2.2: Shear rate vs stress graphs for various fluid types.

Figure 2.2 shows the stress vs shear-rate curves for shear-thinning and shear-thickening behaviour as an exponential decay or increase in the fluid response. Real fluids however asymptote at infinite or zero shear [15], as shown in Figure 2.3.

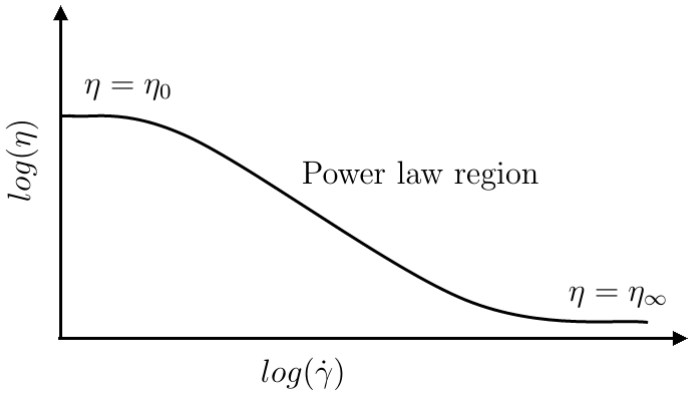

Figure 2.3: Log/log graph of the shear rate dependency of fluids

In Figure 2.3 η_0 is the viscosity at zero shear rate and η_∞ is the limiting viscosity at high shear rates. The power law only holds for the linear region of the log/log graph. In this region the power law fluid behaviour has industrial and experimental importance [15, 16]. The horizontal regions however are difficult to capture.

More complex models which contain the asymptotic regions in Figure 2.3 have been developed; an example is the Carreau model [17], for which the viscosity is

$$\frac{\eta - \eta_\infty}{\eta_0 - \eta_\infty} = \frac{1}{(1 + (\lambda\dot{\gamma})^2)^{(n-1)/2}}.$$

Bingham fluids are a type of Generalised Newtonian fluids that will not flow until a yield stress is exceeded, and otherwise will behave as a rigid or elastic solid. Other types of Generalised Newtonian fluids such as the Cross model, and second-order fluids can be found in texts such as [15, 16].

2.5 Thixotropy

Some fluids exhibit varying viscosity under constant strain-rates. This behaviour is also exhibited in fluids where no viscoelastic effects are present; this is known is thixotropy.

Thixotropic fluids also require a finite time to return to their original state when external loads are removed.

2.6 Viscoelastic Fluids

Viscoelastic fluids exhibit elastic behaviour in combination with viscous behaviour. Viscoelastic fluids however have a fading memory which means that they do not return to their original configuration after undergoing deformation. In [15] experimental results show this kind of behaviour. This behaviour is characterised by time constants, the relaxation and retardation time. The relaxation time refers to the time it takes a fluid to return to a zero stress state after external loads are removed. The retardation time is the time delay in a fluid's response to applied loading conditions.

For viscoelastic fluids an additional term is added to the stress from equation (2.11) to account for elastic effects; this is termed the polymeric or extra stress tensor. The total stress in a viscoelastic fluid then becomes

$$\boldsymbol{S} = p\boldsymbol{I} + \eta\mathbf{D} + \boldsymbol{\tau},$$

where $\boldsymbol{\tau}$ is the extra stess tensor.

2.6.1 Linear Viscoelasticity

The Maxwell fluid is one of the most popular viscoelastic fluids. The fluid model's behaviour can be described by a mechanical analogue of a spring and dash-pot in series as shown in Figure 2.4.

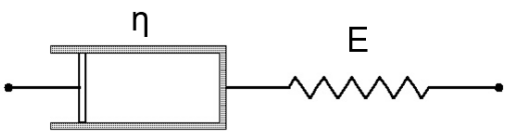

Figure 2.4: Linear viscoelastic Maxwell Model, spring-dashpot model

The elastic and viscous behaviour of the fluid are accounted for by the spring and dashpot respectively. In the series setup the total strain is equal to the sum of the elastic and viscous contributions. The force in each element is equal and given in terms of either the viscous and elastic component

$$F = E\varepsilon_e = \eta\frac{d\varepsilon_\eta}{dt}. \tag{2.14}$$

The rate of change of strain is then given by

$$\begin{aligned}\frac{d\varepsilon}{dt} &= \frac{d\varepsilon_e}{dt} + \frac{d\varepsilon_\eta}{dt} \\ &= \frac{1}{E}\frac{dF}{dt} + \frac{F}{\eta},\end{aligned} \tag{2.15}$$

where F is an applied force and E is the spring constant. Rearranging equation (2.15) we get

$$F + \lambda\frac{dF}{dt} = \eta\frac{d\varepsilon}{dt}, \tag{2.16}$$

where $\lambda = \dfrac{E}{\eta}$ is the relaxation time of the fluid. The generalization of equation (2.16) results in the stress equation for the Maxwell fluid in n dimensions, given by

$$\mathbf{T} + \lambda\frac{\partial\mathbf{T}}{\partial t} = -\eta\boldsymbol{D}. \tag{2.17}$$

The model simplifies to that of a Newtonian fluid for steady flows and resembles a Hookean solid for highly unsteady extra stress. The Maxwell fluid can also be represented in integral as follows:

$$\mathbf{T} = \int_\infty^t \left[\frac{2\eta}{\lambda}e^{-(t-\hat{t})/\lambda}\right]\mathbf{D}(\hat{t})d\hat{t},$$

where $G = \dfrac{2\eta}{\lambda}e^{-(t-\hat{t})/\lambda}$ is the relaxation modulus which describes the fading memory as it decays with increasing time. For this study however the differential form of fluids will be considered as it is the form that will be used in the computational model.

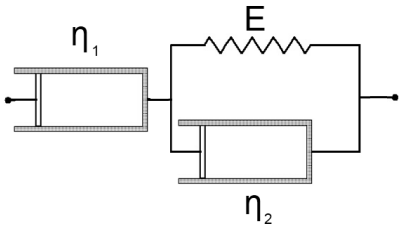

Figure 2.5: Jeffrey Model, spring-dashpot model

Many viscoelastic models have been created by using combinations of springs and dashpots. The Jeffrey model [18], shown in Figure 2.5 is an important example of these models as it employs two time constants, the relaxation and retardation time:

$$\mathbf{T} + \lambda_1 \frac{\partial \mathbf{T}}{\partial t} = -\eta \left(\boldsymbol{D} + \lambda_2 \frac{\partial \boldsymbol{D}}{\partial t} \right). \tag{2.18}$$

Here: $\eta = \eta_1, \quad \lambda_1 = (\eta_1 + \eta_2)/E, \quad \lambda_2 = \eta_2/E.$

The Jeffrey model is also used as the basis for more complex non-linear viscoelastic models.

Other important linear models include the Generalised Maxwell model, the basis for which is a parallel network of a spring in series with a dashpot. The model is used for polymer melts and solvents [15]. Lastly there is the General linear viscoelastic fluid which encompasses the behaviour of most linear viscoelastic models. It is suitable for incompressible viscoelatic flows such as shear flow, elongational flows; however it cannot describe normal shear stress oscillations [15].

2.6.2 Corotational Models

Corotational models are models that are developed by removing the effect of a fluid's rotation. This allows for an objective rheological description of the fluid behaviour. This is done by working with a frame of reference that rotates with the fluid as shown in Figure 2.6.

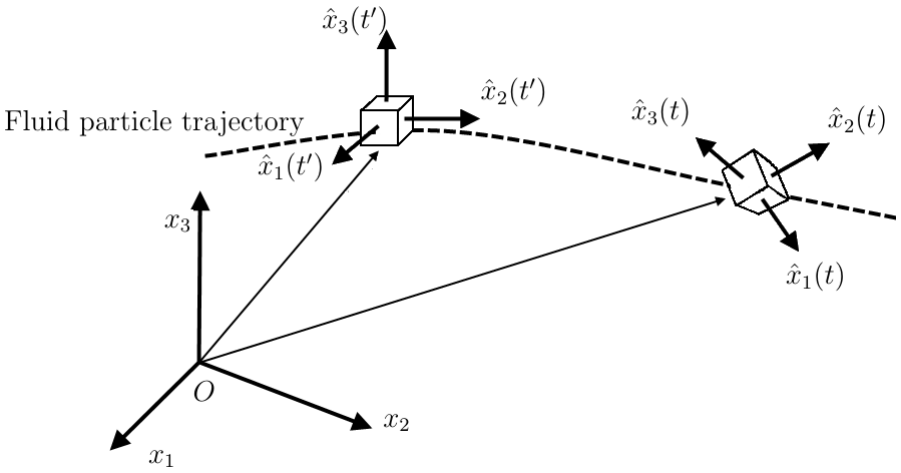

Figure 2.6: Motion of a continuum element in an corotaional frame

These models are suitable for large displacement problems [15]. An example of a linear viscoelastic corotational model is the Jeffrey's model, which is an extension on (2.18), given by

$$\mathbf{T} + \lambda_1 \frac{\mathfrak{D}\mathbf{T}}{\mathfrak{D}t} = -\eta \left(\boldsymbol{D} + \lambda_2 \frac{\mathfrak{D}\boldsymbol{D}}{\mathfrak{D}t} \right),$$

where $\dfrac{\mathfrak{D}\mathbf{T}}{\mathfrak{D}t}$ is the Jaumann or corotational rate, given by

$$\frac{\mathfrak{D}\mathbf{T}}{\mathfrak{D}t} = \frac{D\mathbf{T}}{Dt} + \frac{1}{2}(\boldsymbol{\omega}\mathbf{T} - \mathbf{T}\boldsymbol{\omega}).$$

Further generalisations of the corotational Jeffrey's model were developed to account for additional viscoelastic behaviour. This led to the development of the Oldroyd 8-constant model given by

$$\begin{aligned} &\mathbf{T} + \lambda_1 \frac{\mathfrak{D}\mathbf{T}}{\mathfrak{D}t} + \frac{1}{2}\mu_0(tr(\boldsymbol{\tau})\mathbf{D} - \frac{1}{2}\mu_1 \left(\boldsymbol{D}\mathbf{T} + \mathbf{T}\boldsymbol{D}\right) + \frac{1}{2}\nu_1(\boldsymbol{\tau} : \mathbf{D})\mathbf{I} = \\ &-\eta \left(\boldsymbol{D} + \lambda_2 \frac{\mathfrak{D}\boldsymbol{D}}{\mathfrak{D}t} - \mu_2 \boldsymbol{D}^2 + \frac{1}{2}\nu_2(\mathbf{D} : \mathbf{D})\mathbf{I} \right). \end{aligned} \tag{2.19}$$

Setting certain constants equal to zero leads to various special cases such as the upper convected Maxwell (UCM) and Oldroyd-B model. The UCM model is obtained by setting $\mu_1 = \lambda_1$ and all other constants equal to zero, to give

$$\mathbf{T} + \lambda_1 \overset{\nabla}{\mathbf{T}} = -\eta \boldsymbol{D},$$

where $\overset{\nabla}{(*)}$ is the upper convected derivative defined by

$$\overset{\nabla}{(*)} = \left(\frac{\partial \boldsymbol{u}}{\partial t} + \boldsymbol{u} \cdot \boldsymbol{\nabla}(*) \right) - (\boldsymbol{\nabla u} \cdot (*)) - ((*) \cdot (\boldsymbol{\nabla u})^T).$$

This is the derivative of a fluid property with respect to axis that rotates and stretches with the fluid.

2.7 Oldroyd-B Fluid

The Oldroyd-B fluid is suitable for modelling a polymer in a Newtonian solvent or blood which is a suspension of red and white blood cells and platelets in an aqueous polymer solution [19]. This fluid model is also more suited for shear flows which are appropriate for this study. The constitutive relation for the Oldroyd-B model is given by

$$\mathbf{T} + \lambda_1 \frac{\mathfrak{D}\mathbf{T}}{\mathfrak{D}t} - \frac{1}{2}(\boldsymbol{D}\mathbf{T} + \mathbf{T}\boldsymbol{D}) = -\eta \left(\boldsymbol{D} + \lambda_2 \frac{\mathfrak{D}\boldsymbol{D}}{\mathfrak{D}t} - \lambda_2 \boldsymbol{D}^2 \right)$$

$$\mathbf{T} + \lambda_1 \overset{\nabla}{\mathbf{T}} = -\eta \left(\boldsymbol{D} + \lambda_2 \overset{\nabla}{\boldsymbol{D}} \right).$$

An alternative derivation of the fluid using a Hookean dumbbell model may be found in [16].

2.7.1 Dimensionless Form

As most fluid mechanics problems are treated using dimensionless variables for easier modification and characterisation of behaviour, it is appropriate to use the dimensionless form of the Oldroyd-B equation. Since the Oldroyd-B fluid is used for modelling the behaviour of a polymer in a Newtonian solvent the viscosity is split into the solvent and polymeric viscosity.

The dimensionless constant $\beta = \eta_s/\eta$ which is the ratio of polymeric viscosity to total viscosity, and consequentially the ratio of retardation to relaxation time (λ_2/λ_1), is used to simplify the equation. This results in the momentum and constitutive equations

$$\rho\left(\frac{\partial \boldsymbol{u}}{\partial t}+\boldsymbol{u}\cdot\boldsymbol{\nabla}\boldsymbol{u}\right)+\boldsymbol{\nabla}p-\beta\eta\boldsymbol{\nabla}^2\boldsymbol{u}-\boldsymbol{\nabla}\cdot\boldsymbol{\tau}=0,$$
$$\boldsymbol{\nabla}\cdot\boldsymbol{u}=0,$$
$$\boldsymbol{\tau}+\lambda_1\overset{\nabla}{\boldsymbol{\tau}}-(1-\beta)\eta\boldsymbol{D}=0. \tag{2.20}$$

The dimensionless forms of the various fields are given by

$$\tilde{\boldsymbol{u}}=\frac{\boldsymbol{u}}{U},\quad \tilde{\boldsymbol{x}}=\frac{\boldsymbol{x}}{L},\quad \tilde{t}=\frac{t}{T}=\frac{t}{L/U},$$

where U and L are the characteristic velocity and length. The characteristic time is chosen in terms of the other two as L/U. The dimensionless pressure and extra stress are defined by

$$\tilde{p}=\frac{p}{(U/L)\eta},\quad \tilde{\boldsymbol{\tau}}=\frac{\boldsymbol{\tau}}{(U/L)\eta}.$$

The tildes are now dropped for ease of notation. The resulting dimensionless form of the Oldroyd-B equations is then

$$\mathrm{Re}\left(\frac{\partial \boldsymbol{u}}{\partial t}+\boldsymbol{u}\cdot\boldsymbol{\nabla}\boldsymbol{u}\right)+\boldsymbol{\nabla}p-\beta\boldsymbol{\nabla}^2\boldsymbol{u}-\boldsymbol{\nabla}\cdot\boldsymbol{\tau}=0,$$
$$\boldsymbol{\nabla}\cdot\boldsymbol{u}=0,$$
$$\boldsymbol{\tau}+\mathrm{We}\overset{\nabla}{\boldsymbol{\tau}}-(1-\beta)\boldsymbol{D}=0, \tag{2.21}$$

where: $\mathrm{We}=\dfrac{\lambda_1}{\mathrm{LU}},\quad \mathrm{Re}=\dfrac{\rho\mathrm{UL}}{\eta}.$

The equation involves two additional dimensionless numbers, the Reynolds number Re and the Weissenberg number We. The Reynolds number is the ratio of inertial to viscous forces and is used as a measure of whether a flow is laminar or turbulent. The Weissenberg number is the ratio of viscoelastic to viscous forces and plays an important role as it is a measure of viscoelasticity. An alternative dimensionless number that may be encountered in viscoelastic analysis is the Deborah number De. More details on this number and its relation to the Weissenberg number can be found in [20].

2.8 Other Viscoelastic Models

The Oldroyd-B fluid belongs to a class of fluids known as Boger fluids. These fluids exhibit viscous and elastic behaviour with constant viscosity. This class of fluid is mainly used to analyse the elastic effects in a fluid independently of viscous effects. For more complex behaviour Boger fluids can be generalised to account for non-constant viscosity. Apart from the Oldroyd-B fluid other popular viscoelastic fluids used in literature [16].

Upper Convected Maxwell: The model is a further generalization of spring and dashpot models, this model can be obtained from the Oldroyd 8 constant model.

Giesekus: This model is very similar to the Oldroyd-B fluid but has additional quadratic polymeric-stress terms in its constitutive relation. This model is also obtainable from the Oldroyd 8 constant model.

Johnson-Segalman: This model allows for a non-monotonic relation between the stress and shear-rate. This model allows for different relations in certain flow regions. It is also obtainable from the Oldroyd 8 constant model. Further extension of this model leads to the Phan-Thien-Tanner Model (PTT).

Finite Extensible Nonlinear Elasticity (FENE) The Oldroyd-B fluid experiences limitations in extensional flows as its derivation has Hookean spring-like characteristics, allowing for unlimited extension. The FENE model addresses the infinite extension allowed by the Oldroyd-B fluid and other models by using a non-linear elastic spring with finite extension in its derivation.

Chapter 3

The Finite Element Method

The finite element method (FEM) is a numerical method developed to solve partial differential equations approximately. This method is relevant in the engineering field because many physical phenomena can be modelled using partial differential equations. The method is used in many applications. Introductory material on the finite element method may be found, for example in works by Hughes [21], Fish and Belytscheko [22], and Reddy [23].

This chapter presents an overview of the finite element method. The chapter begins by introducing the variational form of equations. The approximation of the trial and test spaces by finite spaces is then discussed. The partitioning of the domain into elements on which polynomials are used to approximate the solution field is then shown. The interpolation schemes used for these polynomials and how they are constructed are outlined, followed by a description of the reduction to a linear system of algebraic equations.

The later sections of this chapter contain an overview of additional details required to solve mixed finite element problems and time-dependent problems. An extension of the standard methods to a non-standard discontinuous Galerkin method is given. The chapter ends by combining the theory outlined to obtain the discontinuous Galerkin approximation of the Oldroyd-B equations.

3.1 Finite Element Theory

The finite element method may be illustrated using as an example the Poisson's problem:

$$\begin{aligned} -\nabla^2 u &= f \text{ on } \Omega, \\ u &= g \text{ on } \Gamma_D, \\ \nabla u \cdot n &= t \text{ on } \Gamma_N. \end{aligned} \tag{3.1}$$

This is a boundary value problem defined over the domain Ω, with boundary $\partial\Omega$ which is divided into two non-intersecting boundaries Γ_D and Γ_N referred to as the Dirichlet (essential) and Neumann (natural) boundaries where, $\Gamma_D \cup \Gamma_N = d\Omega$ and $\Gamma_D \cap \Gamma_N = \varnothing$.

Here u is a scalar field function, f is an external source term, and g and t are prescribed at the boundary.

3.1.1 Weak Form of The Problem

The Poisson problem given in equation (3.1) is in its strong form. However for the finite element method to be applied the equations must be reformulated in weak (variational) form. Casting the problem into the weak form allows for approximate solutions to the problem to be obtained with fewer restrictions on the derivatives required. To define the weak form we characterise two classes of functions, namely the trial and test (weighting) functions. The trial solutions are required to satisfy the Dirichlet boundary condition $u = g$. Additionally the trial functions and their first derivatives are required to be square integrable, that is they should belong to the first Sobolev space $H^1(\Omega)$, defined by

$$H^1(\Omega) = \left\{ \phi : \int_{-\infty}^{\infty} |\phi|^2 \, d\Omega < \infty \ , \ \int_{-\infty}^{\infty} \left| \frac{\partial \phi}{\partial x} \right|^2 , \left| \frac{\partial \phi}{\partial y} \right|^2 \Omega < \infty \right\}.$$

For nonzero Dirichlet boundary conditions the trial function can be decomposed as $u = u_g + u_0$, where $u_g = g$ and $u_0 = 0$ on the Dirichlet boundary. Therefore the test space is

$$W = \left\{ w \ : \ w \in H^1(\Omega), w = 0 \text{ on } \Gamma_D. \right\}$$

Now that the trial and test functions are defined, the weak form is obtained by multiplying (3.1) by an arbitrary test function $w \in W$ and integrating over the domain Ω to obtain

$$-\int_{\Omega} \boldsymbol{\nabla}^2 u_0 \cdot w \ \ \mathrm{d}\Omega = \int_{\Omega} f w \ \mathrm{d}\Omega. \tag{3.2}$$

In order for the weak form to have only the function u and its first derivatives, integration by parts is used. The resulting boundary terms also introduce natural boundary condition terms. Additionally due to the test functions being zero on the Dirichlet boundary, the boundary terms for Γ_D are zero. The weak form of the equation is then as follows: find $u_0 \in W$ such that

$$\int_\Omega \nabla u_0 \cdot \nabla w \ \ \mathrm{d}\Omega = \int_\Omega fw \ \mathrm{d}\Omega + \int_\Gamma tw \ \ \mathrm{d}\Gamma \quad \forall w \in W. \tag{3.3}$$

Though equation (3.1) requires the second derivatives to be present, it can be shown that the weak form, which only required first derivatives, and the strong form are equivalent if the weak solution is sufficiently smooth [23].

3.1.2 Galerkin Approximation

The Galerkin method is used to obtain approximate solutions to BVPs such as equation (3.3). The infinite dimensional space W is approximated by a finite dimensional space W^h. In the standard Galerkin approximation the trial function is decomposed as $u^h = u_0^h + g^h$, where $u_0^h \in W^h$ and g^h is approximately equal to the Dirichlet boundary conditions: $g^h \approx g$ on Γ_D. Equation (3.3) can now be posed in its discrete form: find $u^h - g^h \in W^h$ such that

$$\int_\Omega \nabla u^h \cdot \nabla w^h \ \ \mathrm{d}\Omega = \int_\Omega fw^h \ \ \mathrm{d}\Omega + \int_\Gamma tw^h \ \ \mathrm{d}\Gamma \quad \forall w^h \in W^h. \tag{3.4}$$

The space W^h is spanned by functions $N_i|_{i=1,2,..n}$, where n is the dimension of the space. Using these functions as a basis, the trial u^h and test w^h functions can be expressed in the form

$$u^h = \sum_{i=1}^{n} d_i N_i \text{ and } w^h = \sum_{j=1}^{n} c_j N_j, \tag{3.5}$$

where d_i and c_i are coefficients. Substitution of (3.5) into equation (3.4) results in

$$\sum_{i=1}^{n}\sum_{j=1}^{n} \int_\Omega d_i \nabla N_i \cdot \nabla c_j N_j \ \ \mathrm{d}\Omega = \sum_{i=1}^{n}\sum_{j=1}^{n} \int_\Gamma t c_j N_j \ \ \mathrm{d}\Gamma + \sum_{j=1}^{n} \int_\Omega f c_j N_j \ \mathrm{d}\Omega; \tag{3.6}$$

that is,

$$c_j \sum_{j=1}^{n} \left(\sum_{i=1}^{n} \left(\int_\Omega \nabla N_i \cdot \nabla N_j \ \mathrm{d}\Omega \right) d_i - \left(\int_\Gamma t N_j \ \mathrm{d}\Gamma + \int_\Omega f N_j \ \mathrm{d}\Omega \right) \right) = 0.$$

Since the test functions are arbitrary the coefficients c_j must be non-zero.

$$\sum_{j=1}^{n} \left(\sum_{i=1}^{n} \left(\int_\Omega \nabla N_i \cdot \nabla N_j \ \mathrm{d}\Omega \right) d_i - \left(\int_\Gamma t N_j \ \mathrm{d}\Gamma + \int_\Omega f N_j \ \mathrm{d}\Omega \right) \right) = 0. \tag{3.7}$$

In equation (3.7) the basis functions are known, leaving d_i as the only unknowns. The problem is then reduced to a system of simultaneous equations which can be written in compact form as

$$\mathbf{A}\boldsymbol{u} = \boldsymbol{b},$$

where

$$A_{ij} = \sum_{j=1}^{n} \sum_{i=1}^{n} \int_\Omega \nabla N_i \cdot \nabla N_j \ \mathrm{d}\Omega,$$
$$b_j = \sum_{j=1}^{n} \left(\int_\Gamma t N_j \ \mathrm{d}\Gamma + \int_\Omega f N_j \ \mathrm{d}\Omega \right).$$

3.1.3 Local Shape Functions

It is difficult to determine suitable basis functions for the Galerkin method for complex domains. The finite element method deals with this by providing a systematic way to construct basis functions for domains with arbitrary shapes [23]. In the finite element method the domain Ω in discretized into non-overlapping elements (Ω_e). The locations where the degrees of freedom of the problem are defined are referred to as nodes. The collection of all elements forms the mesh denoted by $\mathcal{T}^h$, where h is the mesh size.

The basis functions N_i defined in section §3.1.2 are referred to as the global shape functions or interpolation functions. The shape functions allow the field value to be determined at any point in the domain. The restriction of the shape functions N_i to an element in the mesh, Ω_e, is referred to as the local shape function and denoted by

$$N_i|_{\Omega_e} = N_i^e.$$

Local shape functions are defined according to the element choice for the mesh. Popular element choices for two dimensional problems are quadrilateral and triangular elements as shown in Figure 3.1.

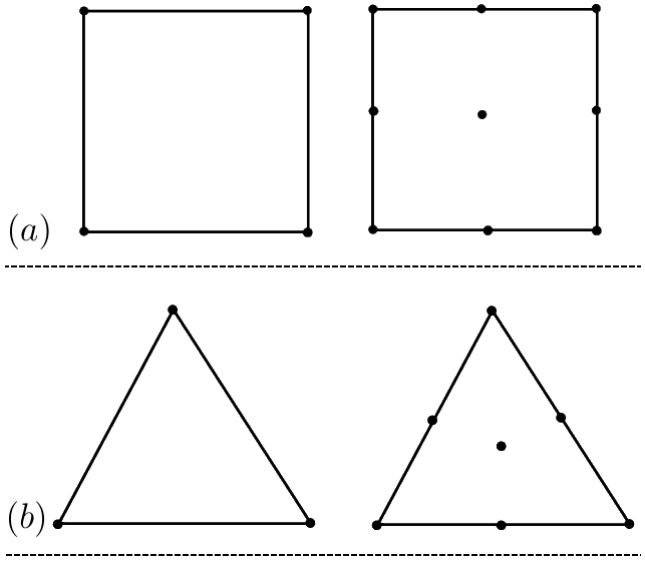

Figure 3.1: Different element types: (a) linear and quadratic quadrilateral elements, (b) linear and quadratic triangular elements.

The coefficients d_i in equation (3.7) represent the degrees of freedom of the element which correspond to the nodes. For the elements shown in Figure 3.1, nodes are placed at least at the vertices. Higher order elements may be obtained by placing nodes at midpoints. The local shape functions for quadrilateral elements, which will be used for the rest of this work, are constructed using Lagrange polynomials between nodes, see section 3.1.4. For the standard Galerkin finite element approach the local shape functions are required to satisfy the following conditions:

- **Continuity**. The shape functions must be bounded and satisfy piecewise continuity between neighbouring elements on shared edges (2D) and faces (3D).
- **Compactness**. The shape functions are zero on elements that do not contain the shape functions corresponding nodes.
- **Completeness**. The shape functions must be capable of approximating the trial and test functions.

- **Kronecker Delta Property**. The shape functions have a value of one at their corresponding nodes and are zero at every other node. This is defined as

$$\delta_{ij} = \begin{cases} 1 & i = j, \\ 0 & i \neq j. \end{cases}$$

Continuity of the shape functions across elements is ensured since the values at the nodes are shared between elements at the interface. The choice of Lagrange polynomials ensures that the functions are continuous.

The quadrilateral elements in Figure 3.1 (a) are denoted as Q_1 and Q_2 where the subscript indicates the polynomial order of the shape functions. For Q_1 elements each nodal value is treated as the coefficients of the bilinear function with the terms $\{1, x, y, xy\}$ which span the shape function N_i^e. Since this element has four degrees of freedom the shape functions satisfy the completeness condition. For higher order elements, such as Q_2, the degrees of freedom correspond to the coefficients of higher order polynomials, $\{1, x, y, xy, x^2, y^2, x^2y, y^2x, x^2y^2\}$ for example in Q_2 elements in 2D.

3.1.4 Lagrange Polynomials

In numerical analysis Lagrange polynomials are used to interpolate between a set of points [22]. This method will produce a unique polynomial of degree $n-1$ that passes through a a given set of points (x_i, y_i) — i = 1,2, ..n. The method produces polynomials using the following product for non-repeating coordinates

$$l_i(x) = \prod_{j \neq i} \left(\frac{x - x_j}{x_i x_j} \right) \tag{3.8}$$

Lagrange interpolation is ideal since it allows for construction of polynomials that satisfy the Kronecker delta property, i.e. the polynomials are one at the associated points and zero at other all points in the set. Figure 3.2 shows shape functions constructed using Lagrange polynomial in 1D.

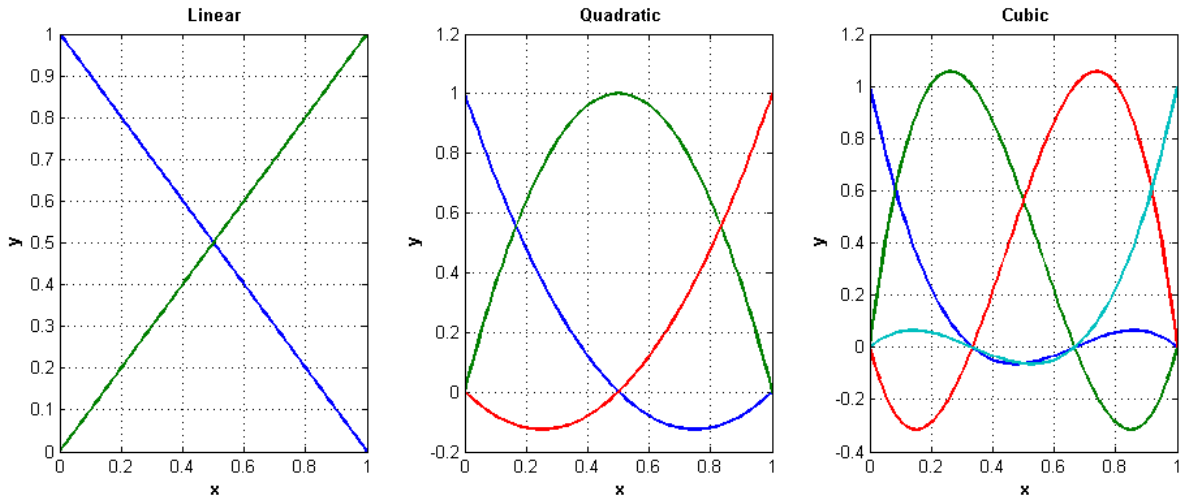

Figure 3.2: 1D Shape functions constructed using Lagrange polynomials

Lagrange polynomials allow shape functions to be extended to higher dimensions by taking the product of functions in each direction.

3.1.5 Reference Frame

In finite elements, most element-wise computations are done in a reference frame. The elements introduced in previous sections are sub-divisions of the real domain, and are defined by the positions of their vertices in the coordinate system of the domain $\boldsymbol{X}^e(x, y)$. The real element is mapped to an isoparametric element in the reference coordinate, $\boldsymbol{\xi} = (\xi, \eta)$ system called the parent element. This mapping is shown in Figure 3.3

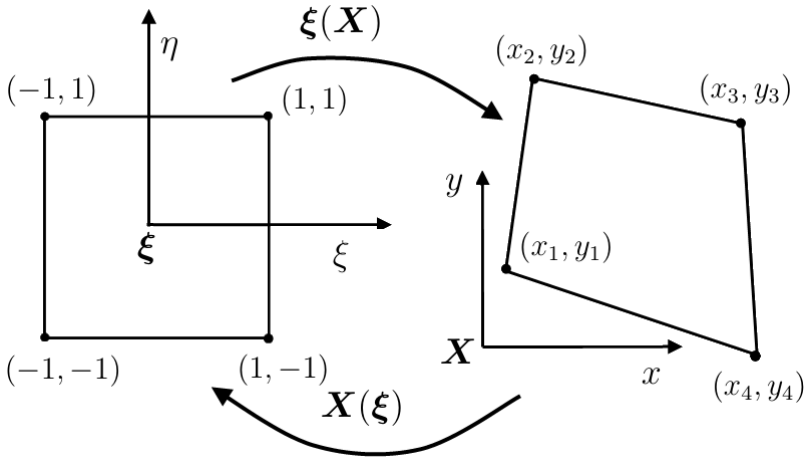

Figure 3.3: An isoparametric mapping between an element in the reference frame ($\boldsymbol{\xi}$) and the real element in the global frame $\boldsymbol{X}$

The parent cell is a bi-unit square as shown in Figure 3.3, where shape function operations

are carried out. The isoparametric mapping from the real cell to the reference cell ($X(\xi) : \xi \rightarrow \xi$) is done using the same shape functions used for interpolation in the previous section. The mapping for a quadrilateral element is given by

$$\boldsymbol{x} = \sum_i \boldsymbol{x}_i \boldsymbol{N}_i(\xi, \eta). \tag{3.9}$$

The parent cell is well suited for Gauss quadrature which is used in finite element to perform numerical integration. The mapping from the real to parent domain is dependent on the corresponding nodes, this ensures that edges on neighbouring cells will be mapped to the same curve in the parent domain. Higher order isoparametric elements allow for construction of elements with curved sides; this is useful in complex engineering structures [22].

3.1.6 Matrix Form

The definitions of the weighting functions and shape functions lead to systems of coupled equations. Rewriting the trial and test functions according to their approximations in equation (3.5) and using the local shape functions in matrix form expressed as

$$\boldsymbol{u} = \boldsymbol{N}\boldsymbol{d} \text{ and } \boldsymbol{w} = \boldsymbol{N}\boldsymbol{c}, \tag{3.10}$$

yields the following Galerkin approximations in terms of element-wise contributions:

$$\sum_{e=1}^{nel} \int_{\Omega^e} \boldsymbol{c}^T (\nabla \boldsymbol{N}^e)^T (\nabla \boldsymbol{N}^e) \boldsymbol{d}^e \ \mathrm{d}\Omega^e - \int_{\Gamma_N^e} \boldsymbol{c}^T (\boldsymbol{N}^e) t \ \mathrm{d}\Gamma_N^e = 0. \tag{3.11}$$

where nel is the number of elements. This gives a system of linear equations with the only unknowns being the vector $\boldsymbol{d}$.

$$\sum_{e=1}^{nel} \int_{\Omega^e} (\nabla \boldsymbol{N}^e)^T (\nabla \boldsymbol{N}^e) \ \mathrm{d}\Omega^e \boldsymbol{d}^e - \int_{\Gamma_N^e} (\boldsymbol{N}^e) t \ \mathrm{d}\Gamma_N^e = 0. \tag{3.12}$$

Compacting the equations further by letting

$$\mathbf{K} = \mathop{\mathbf{A}}_{e=1}^{nel} \int_{\Omega^e} (\nabla \boldsymbol{N}^e)^T (\nabla \boldsymbol{N}^e) \ \mathrm{d}\Omega^e,$$
$$\boldsymbol{b} = \mathop{\mathbf{A}}_{e=1}^{nel} \int_{\Gamma_N^e} (\boldsymbol{N}^e) t \ \mathrm{d}\Gamma_N^e = 0.$$

Here $\overset{nel}{\underset{e=1}{\mathbf{A}}}$ is the assembly operator. Adding all elemental contributions yields the following linear system of equations in matrix form as

$$\mathbf{K}\boldsymbol{u} = \boldsymbol{b}.$$

The finite element method yields a matrix $\boldsymbol{A}$ that is sparse with entries concentrated around the diagonal. For the example used here, the matrix is also symmetric. These properties are often used to advantage in the algorithms used to assemble the systems of equations as well as those employed to solve the system of equations.

3.1.7 Mixed Finite Elements

The problem used to illustrate the finite element method is previous sections was for a scalar valued field ϕ. For fields that are vector or tensor valued the same method is applicable, with each component being treated as a different field. When handling problems that deal with complex behaviour the systems involved generally result in a mixed finite element problem. Additional work for these types of problems comes from ensuring stability in the system.

In this work, both vector and tensor valued fields are used as well as a scalar field, resulting in a mixed problem. An example of a mixed formulation is the Stokes problem

$$\begin{aligned} -\eta\boldsymbol{\nabla}^2\boldsymbol{u} + \boldsymbol{\nabla}p &= \boldsymbol{b}, \\ \boldsymbol{\nabla}\cdot\boldsymbol{u} &= \mathbf{0}, \\ \boldsymbol{u}|_\Gamma &= 0, \end{aligned} \tag{3.13}$$

where $\boldsymbol{u}$ is the velocity, p is the pressure, $\boldsymbol{b}$ is an external load and η is the fluid viscosity. The spaces for the fields $\boldsymbol{u}$ and p are defined as

$$\begin{aligned} U &= \left\{\boldsymbol{u} \ : \ \boldsymbol{u} \in [H^1(\Omega)]^d, \boldsymbol{u} = 0 \text{ on } \Gamma_D\right\}, \\ Q &= \left\{p \ : \ p \in L^2(\Omega)\right\}. \end{aligned}$$

Here d is the spatial dimension of the problem. The weak formulation of equation (3.13) is then as follows: find $\boldsymbol{u} \in U$ and $p \in Q$ such that

$$\int_\Omega \boldsymbol{\nabla w} : \nabla \boldsymbol{u} \, \mathrm{d}\Omega + \int_\Omega p \boldsymbol{\nabla} \cdot \boldsymbol{w} \, \mathrm{d}\Omega = \int_\Omega \boldsymbol{b} \cdot \boldsymbol{w} \, \mathrm{d}\Omega \quad \forall \boldsymbol{w} \in U,$$
$$\int_\Omega q \boldsymbol{\nabla} \cdot \boldsymbol{u} \, \mathrm{d}\Omega = \boldsymbol{0} \quad \forall q \in Q. \tag{3.14}$$

In this formulation $\boldsymbol{w}$ and q are the test functions for the velocity and pressure field respectively. The pressure is a Lagrange multiplier enforcing the incompressibility constraint.

The discrete spaces for the problem using the Galerkin method are $U^h \subset U$ and $Q^h \subset Q$. Applying the standard Galerkin finite element method on (3.14) leads to systems of equations with the following block matrix form:

$$\begin{pmatrix} \boldsymbol{A} & \boldsymbol{B} \\ \boldsymbol{B}^T & 0 \end{pmatrix} \begin{pmatrix} \boldsymbol{d} \\ \boldsymbol{p} \end{pmatrix} = \begin{pmatrix} b \\ 0 \end{pmatrix}$$

A problem of this nature is known as a saddle point problem. The choice of spaces chosen for $\boldsymbol{u}$ and p are subject to the Ladyzhenskaya-Babuska-Brezzi (LBB) condition to ensure stability. For more on this condition see [24, 25]. The incompressible Naviers-Stokes equation, and Oldroyd-B system of equations in Chapter 2 are also subject to a similar compatibility requirement due to the incompressibility requirement. For the Stokes problem, a stable pair elements is $Q_2 - P_1^{disc}$ for the velocity and pressure fields respectively, here P_1^{disc} is a piecewise discontinuous linear element.

3.1.8 Time-Dependent Methods

Attention so far has been focused on steady problems. In order to solve transient problems using the finite element method a time discretization method is required. Time is partitioned into intervals $t_0 = 0 < t_1 < t_2 < ... < t_N = T$. The time step is denoted by $\Delta t = t_n - t_{n-1}$. The field value at time t is similarly denoted as $u^n = u(t_n)$. The time derivative of a field is written as a function of its value at the previous time step $u(t) = u^{n-1}$ and its value at the current time step $u(t + \Delta t) = u^n$ according to

$$\frac{u^n - u^{n-1}}{\Delta t} = (1 - \theta)a^{n-1} + \theta a^n, \tag{3.15}$$

where $a = \dfrac{\partial u}{\partial t}$. The parameter θ is a constant in the range $[0, 1]$. Three of the most common choices of θ are,

- $\theta = 0$: fully explicit Forward Euler scheme. This scheme results in an explicit

expression for the solution at the next time step. The Forward Euler scheme however is not unconditionally stable. The time step is limited by the the square of the discretization size h^2. This means that for finer meshes the time step is very small, making it computationally expensive for longer time periods.

- $\theta = 1$: fully implicit Backward Euler scheme. The scheme is unconditionally stable and has $O(\Delta t)$ accuracy. The disadvantage of this scheme is that the system matrix will need to be inverted at every time step, which is computationally expensive.
- $\theta = \frac{1}{2}$: Crank Nicholson scheme. The scheme is $O(\Delta t^2)$ accurate and unconditionally stable. The method however is computationally expensive as all terms in the scheme require matrix inversion operations.

For this work the Backward Euler scheme will be used to avoid restrictions placed on stability of the scheme.

3.2 Discontinuous Galerkin Method

Discontinuous Galerkin methods are a class of finite element methods where the continuity requirement across elements is relaxed. The method was introduced by Reed and Hill in 1974 [26] and by Lesaint and Raviat [27] in 1974, to solve the neutron transport problem. The Discontinuous Galerkin method offers various advantages such as the ability to handle complex geometries easily, incorporating refinement which may result in neighbouring elements having differing polynomial orders, or multiple cells sharing the same interface with one element (*hp*-refinement). Furthermore it can be easily parallelized. A more important advantage is that the method is capable of capturing discontinuous solutions that arise from some hyperbolic problems. Additionally, the method allows for solutions to be determined on an element-by-element basis.

Discontinuous Galerkin Methods were first used to solve for viscoelastic flows by Fortin and Fortin [28]. For this work the relevant Discontinuous Galerkin method uses DG-upwinding; see also [8, 6] for its use in the Oldroyd-B model. The reason is that standard Galerkin methods result in unstable solutions for advection dominated problems. In this work one such term arises in the constitutive relation for the extra stress which is in the form of an advection-reaction problem. To illustrate DG-upwinding consider the scalar advection-reaction problem

$$2\mathbf{k} \cdot \nabla u - u = 0, \tag{3.16}$$

where u is the unknown scalar field and $\boldsymbol{k}$ is a known flux on the inlet boundary. Various terms relating to the interface are defined and shown in Figure 3.4.

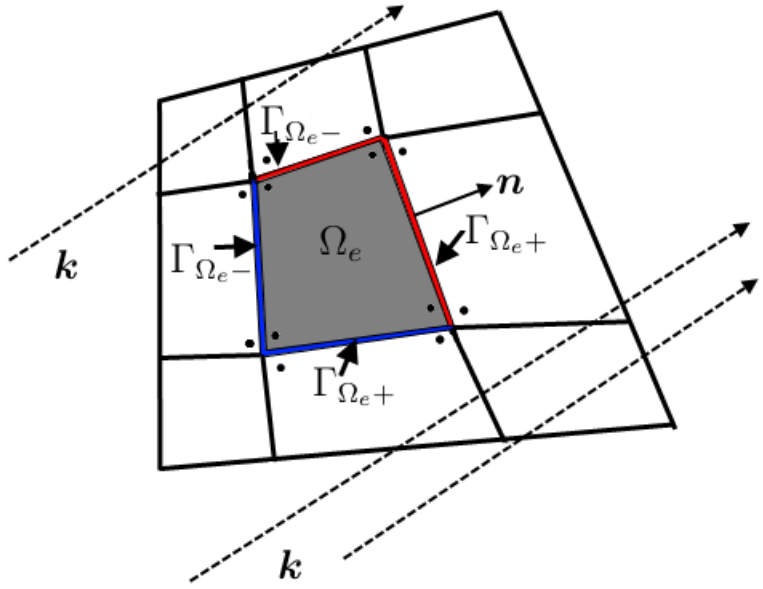

Figure 3.4: A Q_1^{disc} element Ω_e used for discontinuous Galerkin in an advective field $\boldsymbol{k}$ with inflow boundaries Γ_{K-} (blue) and outflow boundaries Γ_{K+}.

The boundaries of the element are divided into two groups, the inflow Γ_{Ω_e-} (upwind) and outflow Γ_{Ω_e+} (downwind) boundaries based on the convective field $\boldsymbol{k}$. A boundary is defined as upwind if

$$\boldsymbol{k} \cdot \boldsymbol{n} < 0,$$

while for a downwind boundary

$$\boldsymbol{k} \cdot \boldsymbol{n} > 0.$$

The value of the field on the cell that is "upwind" of the interface is denoted by u^- and the downwind value by u^+; similarly, the respective outward normals are denoted by $\boldsymbol{n}^-$ and $\boldsymbol{n}^+$. DG-upwinding is applied only to the advective term by integrating by parts with the resulting boundary terms treated as the contributions from the inflow boundary at the cell. Thus

$$\int_{\Gamma_{\Omega_e-}} (2\mathbf{k}u^- \cdot \mathbf{n}^- w^-) \, \mathrm{d}\Gamma_{\Omega_e-} - \int_{\Omega_e} (u(2\mathbf{k} \cdot \nabla w) \, \mathrm{d}\Omega_e - \int_{\Omega_e} (w \cdot u) \, \mathrm{d}\Omega_e = 0.$$

The integral over Ω_e is then integrated by parts a second time, resulting in the expression returning to its original form with an additional boundary term, which is treated as a contribution from the outflow boundary of the cell. This gives

$$\int_{\Gamma_{\Omega_e+}} (2\mathbf{k}u^+ \cdot \mathbf{n}^+ w^+) d\Gamma_{\Omega_e+} - \int_{\Gamma_{\Omega_e-}} (2\mathbf{k}u^- \cdot \mathbf{n}^- w^-) \, \mathrm{d}\Gamma_{\Omega_e-} + \int_{\Omega_e} (w(2\mathbf{k} \cdot \nabla u) \, \mathrm{d}\Omega_e - \int_{\Omega_e} (w \cdot u) \, \mathrm{d}\Omega_e = 0.$$

The expression can be rewritten in compact form by defining the jump $[\![u]\!]$ by

$$[\![u]\!] = u^+ - u^-.$$

Given that the shape functions are the same for both cells across the interface, the resulting equation is then

$$\int_{\Gamma_{\Omega_e}} (2\mathbf{k}w^- \cdot [\![u]\!]) \, \mathrm{d}\Gamma_{\Omega_e} + \int_{\Omega_e} (w(2\mathbf{k} \cdot \nabla u) \, \mathrm{d}\Omega_e - \int_{\Omega_e} (w \cdot u) \, \mathrm{d}\Omega_e = 0.$$

It is important to note that when using piecewise-constant discontinuous approximations the gradient term is zero, while the jump terms still have a contribution. In this work weakly enforced boundary condition will be used for the constitutive relation. These boundary conditions are enforced as follows for $u = g$ on Γ_D:

$$\int_{\Gamma_D} wu \, d\Gamma = \int_{\Gamma_D} wg \, d\Gamma$$

-

3.3 DG Formulation of Oldroyd-B Model

The methods outlined in the previous sections will now be used to derive the DG formulation for the Oldroyd-B equations.

The Oldroyd-B equation (2.21) is first discretized in time before obtaining the weak form. After the weak form is obtained the Discontinuous Galerkin method is applied. Discretization of equation (2.21) in time using the Backward Euler scheme yields

$$\frac{\mathrm{Re}}{\Delta t}\boldsymbol{u}^n + \mathrm{Re}(\nabla \boldsymbol{u}^n \cdot \boldsymbol{u}^n) + \nabla p^n - \beta \nabla^2 \boldsymbol{u}^n - \nabla \cdot \boldsymbol{\tau}^n = \frac{\mathrm{Re}}{\Delta t}\boldsymbol{u}^{n-1},$$
$$\nabla \cdot \boldsymbol{u}^n = 0,$$
$$\left(1 + \frac{\mathrm{We}}{\Delta t}\right)\boldsymbol{\tau}^n + \mathrm{We}(\nabla \boldsymbol{\tau}^n \cdot \boldsymbol{u}^n) - \nabla \boldsymbol{u}^n \cdot \boldsymbol{\tau}^n - \boldsymbol{\tau}^n \cdot (\nabla \boldsymbol{u}^n)^T$$
$$-(1-\beta)(\nabla \boldsymbol{u}^n + \nabla \boldsymbol{u}^{nT}) = \frac{\mathrm{We}}{\Delta t}\boldsymbol{\tau}^{n-1}.$$

The spaces for the solution fields are chosen as

$$U = \left\{\boldsymbol{u} \ : \ \boldsymbol{u} \in [H^1(\Omega)]^d, \boldsymbol{u} = 0 \text{ on } \Gamma_D\right\},$$
$$Q = \left\{p \ : \ p \in L^2(\Omega)\right\},$$
$$S = \left\{\boldsymbol{\tau} \ : \ \boldsymbol{\tau} \in [L^2(\Omega)]^{d^2}, \boldsymbol{\tau} = 0 \text{ on } \Gamma_{in}\right\}.$$

where, $\boldsymbol{u}$ is the velocity field, p the pressure field, and $\boldsymbol{\tau}$ the extra-stress field. Here we have assumed homogeneous boundary conditions for convenience. The weak form for the momentum equation is obtained by multiplying by an arbitrary test function $\boldsymbol{w} \in U$ and integrating over an element. Integration by parts gives the weak form

$$\begin{aligned}
&\int_{\Omega_e} \frac{\mathrm{Re}}{\Delta t}\boldsymbol{u}^n \cdot \boldsymbol{w} \ \partial\Omega_e + \int_{\Omega_e} \mathrm{Re}\nabla \boldsymbol{u}^n \cdot \boldsymbol{u}^n \cdot \boldsymbol{w} \ \partial\Omega_e - \int_{\Omega_e} p^n(\nabla \cdot \boldsymbol{w}) \ \partial\Omega_e \\
&+ \int_{\Omega_e} \beta \nabla \boldsymbol{u}^n \cdot \nabla \boldsymbol{w} \ \partial\Omega_e + \boldsymbol{\tau}^n \cdot \nabla \boldsymbol{w} \ \partial\Omega_e \\
&= \int_{\Omega_e} \frac{\mathrm{Re}}{\Delta t}\boldsymbol{u}^{n-1} \cdot \boldsymbol{w} \ \partial\Omega_e + \int_{\Gamma_N \cap \partial\Omega_e} (-p^n \boldsymbol{I} \cdot \boldsymbol{n} + \beta \nabla \boldsymbol{u}^n \cdot \boldsymbol{n} + \boldsymbol{\tau}^n \cdot \boldsymbol{n}) \cdot \boldsymbol{w} \ \partial\Gamma_N. \qquad (3.17)
\end{aligned}$$

The incompressibility constraint is similarly multiplied by a test function $q \in Q$ and integrated to give

$$\int_{\Omega_e} (\nabla \cdot \boldsymbol{u}^n)\, q \ \partial\Omega_e = 0. \qquad (3.18)$$

The weak form of the constitutive relation is obtained by taking the scalar product of equation (2.21) with the test function $\boldsymbol{\sigma}$ to give

$$\int_{\Omega_e} \left(1 + \frac{\mathrm{We}}{\Delta t}\right) \boldsymbol{\tau}^n : \boldsymbol{\sigma} + \int_{\Omega_e} \mathrm{We}(\nabla \boldsymbol{\tau}^n \cdot \boldsymbol{u}^n) : \boldsymbol{\sigma}\ \partial\Omega_e$$
$$- \int_{\Omega_e} (\nabla \boldsymbol{u}^n \cdot \boldsymbol{\tau}^n + \boldsymbol{\tau}^n \cdot (\nabla \boldsymbol{u}^n)^T) : \boldsymbol{\sigma}\ \partial\Omega_e$$
$$- \int_{\Omega_e} (1-\beta)(\nabla \boldsymbol{u}^n : \boldsymbol{\sigma} + (\nabla \boldsymbol{u}^n)^T : \boldsymbol{\sigma})\ \partial\Omega_e = \int_{\Omega_e} \left(\frac{\mathrm{We}}{\Delta t}\right) \boldsymbol{\tau}^{n-1} : \boldsymbol{\sigma}\ \partial\Omega_e. \tag{3.19}$$

DG-upwinding is then applied to the advective term in the constitutive relation to yield

$$\int_{\Omega_e} \left(1 + \frac{\mathrm{We}}{\Delta t}\right) \boldsymbol{\tau}^n : \boldsymbol{\sigma}\ \partial\Omega_e + \int_{\Omega_e} \mathrm{We}(\nabla \boldsymbol{\tau}^n \cdot \boldsymbol{u}^n) : \boldsymbol{\sigma}\ \partial\Omega_e$$
$$- \int_{\Omega_e} (\nabla \boldsymbol{u}^n \cdot \boldsymbol{\tau}^n + \boldsymbol{\tau}^n \cdot (\nabla \boldsymbol{u}^n)^T) : \boldsymbol{\sigma}\ \partial\Omega_e$$
$$- \int_{\Omega_e} (1-\beta)(\nabla \boldsymbol{u}^n : \boldsymbol{\sigma} + (\nabla \boldsymbol{u}^n)^T : \boldsymbol{\sigma})\ \partial\Omega_e$$
$$= \int_{\Omega_e} \left(\frac{\mathrm{We}}{\Delta t}\right) \boldsymbol{\tau}^{n-1} : \boldsymbol{\sigma}\ \partial\Omega_e - \int_{\Gamma_e} \mathrm{We}(\boldsymbol{u}^{n+} \cdot \boldsymbol{n}^+)[\![\boldsymbol{\tau}^n]\!] : \boldsymbol{\sigma}^+\ \partial\Gamma_e. \tag{3.20}$$

The element choices based on the discussion section 3.1.8 are $Q_2 - P_1^{disc}$ for the velocity and pressure fields respectively. A stable set of elements is chosen according to [8] where Crouzeix-Raviart triangular elements were used, the quadratic analogue was used by Donea and Heurta [29], and Fortin[30], as well by [6]. In this work biquadratic (2D) and triquadratic (3D) elements are chosen for the velocity, and linear discontinuous elements for pressure.

In addition to the LBB condition, Fortin and Pierre [31] have shown that if the model does not have a solvent viscosity and Lagrangian polynomials are used for interpolation, the rate of deformation $\boldsymbol{D}$, and the gradient of the velocity $\nabla \boldsymbol{u}$, must lie in the same space as the extra-stress tensor. An outline of element choices required for stability is given in [32]. In this work the solvent viscosity is non-zero so a lower order element for the extra-stress will also be considered, based on [6].

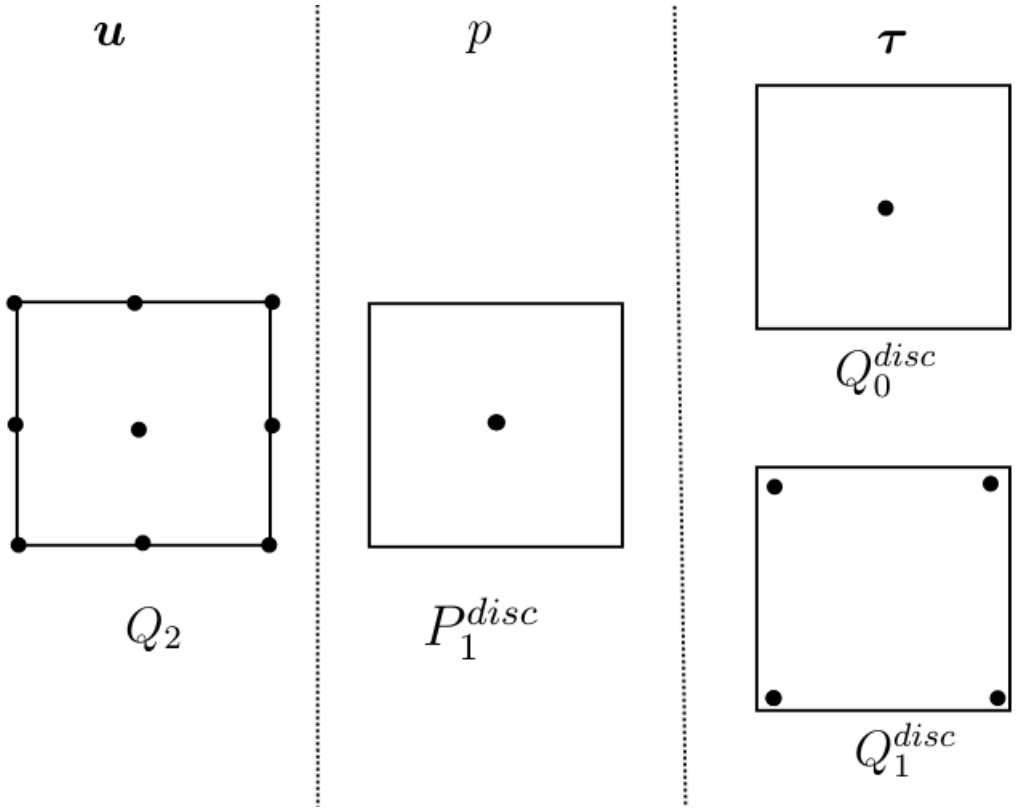

Figure 3.5: Element choices for the three different fields of the Oldroyd-B model ($\boldsymbol{u}$, p and $\boldsymbol{\tau}$)

Figure 3.5 shows the element choice for the Oldroyd-B model. For the extra stress field we use piecewise constant discontinuous Q_0^{disc} or bilinear discontinuous Q_1^{disc} elements, as shown in Figure 3.5. Q_0^{disc} elements are considered based on [8, 6, 33], where these are shown to be stable.

Following the Galerkin method the trial and test spaces are approximated by finite dimensional spaces U^h, Q^h and S^h:

$$
\begin{aligned}
U^h &= \left\{ \boldsymbol{u} \ : \ \boldsymbol{u} \in [C(\Omega)]^d, \boldsymbol{u}^h|_{\Omega_e} \in Q_2 \right\}, \\
Q^h &= \left\{ p^h \ : \ p^h \in L^2(\Omega), p^h|_{\Omega_e} \in P_1^{disc} \right\}, \\
S^h &= \left\{ \boldsymbol{\tau}^h|_{\Omega_e} \ : \ \boldsymbol{\tau}^h|_{\Omega_e} \in [L^2(\Omega)]^{d^2}, \boldsymbol{\tau}^h|_{\Omega_e} \in Q_0^{disc} \text{ or } \boldsymbol{\tau}^h \in Q_1^{disc} \right\}.
\end{aligned}
$$

To make it easier to read the superscript h is dropped, leaving n, the time step index, as the only superscript in the equations. The weak form of the system of equations at time step n is then given as follows:

- Given $(\boldsymbol{u}^{n-1}, \boldsymbol{\tau}^{n-1})$ find $\boldsymbol{u}^n \in U^h$, $p \in Q^h$ and $\boldsymbol{\tau} \in S^h$ such that equations (3.17), (3.18) and (3.20) hold for all $\boldsymbol{w}^n \in U^h$, $q \in Q^h$ and $\boldsymbol{\sigma} \in S^h$ respectively.

The systems of equations for the Oldroyd-B system yield the following block matrix form:

$$\begin{pmatrix} \boldsymbol{A}(\boldsymbol{u}) & \boldsymbol{B}(\boldsymbol{u},p) & \boldsymbol{C}(\boldsymbol{u},\boldsymbol{\tau}) \\ \boldsymbol{B}^T(p,\boldsymbol{u}) & 0 & 0 \\ \boldsymbol{D}(\boldsymbol{\tau},\boldsymbol{u}) & 0 & \boldsymbol{E}(\boldsymbol{\tau}) \end{pmatrix} \begin{pmatrix} \boldsymbol{u} \\ p \\ \boldsymbol{\tau} \end{pmatrix} = \begin{pmatrix} \boldsymbol{F}_1(\boldsymbol{u},p,\boldsymbol{\tau}) \\ \boldsymbol{0} \\ \boldsymbol{F}_3(\boldsymbol{u},\boldsymbol{\tau}) \end{pmatrix}$$

The system obtained however is non-linear. The method outlined in this chapter is not sufficient to solve this type of problem without additional numerical methods being employed. The additional numerical methods required and the algorithm implemented will be discussed in the next chapter.

Chapter 4

Solution Methods

This chapter is concerned with the numerical methods required to solve the discrete Oldroyd-B equations and their implementation. A description of the Newton-Raphson method for solving non-linear problems is given. An algorithm for the method's implementation is also given. The method is then used to derive the linearisation of the equations for the Oldroyd-B model. The use of a line search with the Newton-Raphson method is described next. The heuristic method used to adjust the damping constant in the line search is shown in algorithmic form.

The remainder of the sections deal with the functionality provided by the deal.ii finite element library. The implementation of the finite element problem is described. The chapter ends with an outline of the adaptive mesh refinement scheme used and a discussion of parallel computing methods.

4.1 Nonlinear Finite Elements

The systems of equations arrived at in section §3.3 are non-linear and thus the solution cannot be obtained directly. The system can be solved by linearising and solving with an iterative method. The most common methods applied in the finite element context are fixed point methods such as Picard iteration, and the Newton-Raphson method [34]. The Picard method is easy to implement and is computationally inexpensive per iteration; however, it converges slowly [35]. The Newton-Raphson method, though more computationally expensive per iteration, converges faster. The Newton-Raphson method has a quadratic convergence rate under appropriate conditions [34], compared to linear convergence for the Picard method. The Newton-Raphson method is more robust and stable as shown in [16], where it converges for higher Weissenburg numbers.

4.1.1 The Newton Raphson Method

The Newton-Raphson method is one of the most frequently used schemes for solving systems of nonlinear algebraic equations[34]. To derive the method we consider a system of equations $\boldsymbol{R}(\boldsymbol{u}) = \boldsymbol{0}$ where $\boldsymbol{u}$ represents the vector of unknowns. The Taylor series expansion around the initial guess $\boldsymbol{u}_0$ is given by

$$R_i(\boldsymbol{u}) = R_i(\boldsymbol{u}_0) + \sum_j \frac{\partial R_i}{\partial u_j}(u_j - u_{0j}) + \frac{1}{2!}\sum_j \sum_k \frac{\partial^2 R_i}{\partial u_j \partial u_k}(u_j - u_{0j})(u_k - u_{0k}) + ... \quad (4.1)$$

Dropping the higher order terms, we obtain

$$\boldsymbol{R}(\boldsymbol{u}^{i+1}) \simeq \boldsymbol{R}(\boldsymbol{u}^i) + \frac{\partial \boldsymbol{R}(\boldsymbol{u}^i)}{\partial \boldsymbol{u}}(\boldsymbol{u}^{i+1} - \boldsymbol{u}^i). \quad (4.2)$$

Setting $\boldsymbol{R}(\boldsymbol{u}^{i+1}) = \boldsymbol{0}$ we obtain

$$\begin{aligned} \frac{\partial \boldsymbol{R}(\boldsymbol{u}^i)}{\partial \boldsymbol{u}}(\delta \boldsymbol{u}) &= -\boldsymbol{R}(\boldsymbol{u}^i) \\ \boldsymbol{u}^{i+1} &= \delta \boldsymbol{u} + \boldsymbol{u}^i. \end{aligned} \quad (4.3)$$

The matrix $\dfrac{\partial \boldsymbol{R}(\boldsymbol{u}^i)}{\partial \boldsymbol{u}}(\delta \boldsymbol{u})$ is referred to as the tangent and $\boldsymbol{R}(\boldsymbol{u}^i)$ is the residual vector. The tangent is computed as follows:

$$\frac{\partial \boldsymbol{R}(\boldsymbol{u}^i)}{\partial \boldsymbol{u}}(\delta \boldsymbol{u}) = \frac{\partial \boldsymbol{R}(\boldsymbol{u}^i + \epsilon \delta \boldsymbol{u})}{\partial \epsilon}. \quad (4.4)$$

The algorithm is executed as follows:

Algorithm 1: Newton-Raphson Scheme

1 compute the residual $\boldsymbol{R}(\boldsymbol{u}^i)$ and the shape functions for $\dfrac{\partial \boldsymbol{R}(\boldsymbol{u}^i)}{\partial \boldsymbol{u}}(\delta \boldsymbol{u})$
2 compute $\delta \boldsymbol{u}$
3 compute $\boldsymbol{u}^{i+1} = \delta \boldsymbol{u} + \boldsymbol{u}^i$
4 **if** $\boldsymbol{R}(\boldsymbol{u}^{i+1})$ *is within an acceptable tolerance* **then**
5 | stop
6 **else**
7 | increase iteration counter : $i = i + 1$
8 | update $\boldsymbol{u}^i$
9 **end**
10 repeat from step 1

4.1.2 Linearised Oldroyd-B Problem

Using the Newton-Raphson method with initial guesses $\boldsymbol{u}_0$, p_0 and $\boldsymbol{\tau}_0$ the tangent for the Oldroyd-B eqations is obtained. The contribution of the momentum equation (3.17), at time step t^n, is given by:

$$\begin{aligned}
&\int_\Omega \frac{\mathrm{Re}}{\Delta t}\delta \boldsymbol{u}^n \cdot \boldsymbol{w} + \mathrm{Re}(\nabla \delta \boldsymbol{u}^n \cdot \boldsymbol{u}_0^n + \nabla \boldsymbol{u}_0^n \cdot \delta \boldsymbol{u}^n) \cdot \boldsymbol{w} \; \partial\Omega \\
&+ \int_\Omega -\delta p^n (\nabla \cdot \boldsymbol{w}) + \beta \nabla \delta \boldsymbol{u}^n \cdot \nabla \boldsymbol{w} + \delta \boldsymbol{\tau}^n \cdot \nabla \boldsymbol{w} \; \partial\Omega \\
&= \int_\Omega \frac{\mathrm{Re}}{\Delta t}\boldsymbol{u}^{n-1} \cdot \boldsymbol{w} \; \partial\Omega + \int_{\Gamma_N} (-\delta p^n \boldsymbol{I} \cdot \boldsymbol{n} + \beta \nabla \delta \boldsymbol{u}^n \cdot \boldsymbol{n} + \delta \boldsymbol{\tau}^n \cdot \boldsymbol{n}) \cdot \boldsymbol{w} \; \partial\Gamma_N. \qquad (4.5)
\end{aligned}$$

The contribution of the incompressibility constraint (3.18) to the tangent is accounted for by adding the following:

$$\int_\Omega (\nabla \cdot \delta \boldsymbol{u}^n)\, q \; \partial\Omega = 0 \qquad (4.6)$$

Secondly the contribution of the constitutive equation (3.20) is given by

$$
\begin{aligned}
&\int_{\Omega_e} \left(1 + \frac{\mathrm{We}}{\Delta t}\right) \delta\boldsymbol{\tau}^n : \boldsymbol{\sigma} + \mathrm{We}((\nabla\delta\boldsymbol{\tau}^n) \cdot \boldsymbol{u}_0^n + (\nabla\boldsymbol{\tau}_0^n) \cdot \delta\boldsymbol{u}^n) : \boldsymbol{\sigma}\ \partial\Omega_e \\
&- \int_{\Omega_e} \left(\nabla\delta\boldsymbol{u}^n\boldsymbol{\tau}_0^n + \nabla\boldsymbol{u}_0^n\delta\boldsymbol{\tau}^n + \delta\boldsymbol{\tau}^n(\nabla\boldsymbol{u}_0^n)^T + \boldsymbol{\tau}_0^n(\nabla\delta\boldsymbol{u}^n)^T\right) : \boldsymbol{\sigma}\ \partial\Omega_e \\
&- \int_{\Omega_e} (1-\beta)(\nabla\delta\boldsymbol{u}^n : \boldsymbol{\sigma} + (\nabla\delta\boldsymbol{u}^n)^T : \boldsymbol{\sigma})\ \partial\Omega_e \\
&= \int_{\Omega_e} \left(\frac{\mathrm{We}}{\Delta t}\right) \boldsymbol{\tau}^{n-1} : \boldsymbol{\sigma}\ \partial\Omega_e - \int_{\Gamma_e} \mathrm{We}((\delta\boldsymbol{u}^{n+} \cdot \boldsymbol{n}^+)[\![\boldsymbol{\tau}_0^n]\!] + (\boldsymbol{u}_0^{n+} \cdot \boldsymbol{n}^+)[\![\delta\boldsymbol{\tau}^n]\!]) : \boldsymbol{\sigma}^+\ \partial\Gamma_e.
\end{aligned}
\tag{4.7}
$$

The residual is given by substituting the initial guesses ($\boldsymbol{u}_0$, p_0 ,$\boldsymbol{\tau}_0$) into equations (3.17), (3.18) and (3.20).

4.1.3 Line Search

Convergence of the Newton-Raphson scheme however is not guaranteed. If the initial guess is close a solution the scheme converges locally in the region of the initial guess [34] and there may be more than one solution for non-linear problems. Without the appropriate initial guess the scheme may diverge or converge to the wrong solution.

Damping can be applied to the update of the solution $\delta\boldsymbol{u}$ to ensure that the scheme tends towards a solution in the region of the initial guess. A damping parameter α, which is limited to a value between 0 and 1, is applied to the solution update as follows:

$$\boldsymbol{u}^{i+1} = \alpha\delta\boldsymbol{u} + \boldsymbol{u}^i$$

Mathematical models for determining α may be found in [34, 36]; however, such models can be computationally expensive. For this work a heuristic approach is applied due to the simplicity of its application and its relatively low computational cost. The algorithm for the self-adjusting parameter is applied as follows:

Algorithm 2: Modified Newton-Raphson Scheme

1 set $\alpha = 1$
2 compute the residual $\boldsymbol{R}(\boldsymbol{u}^i)$ and the shape functions for $\dfrac{\partial \boldsymbol{R}(\boldsymbol{u}^i)}{\partial \boldsymbol{u}}(\delta \boldsymbol{u})$
3 compute $\delta \boldsymbol{u}$
4 compute $\boldsymbol{u}^{i+1} = \alpha \delta \boldsymbol{u} + \boldsymbol{u}^i$
5 compute $\dfrac{\partial \boldsymbol{R}(\boldsymbol{u}^{i+1})}{\partial \boldsymbol{u}}(\delta \boldsymbol{u})$
6 **if** $\left|\dfrac{\partial \boldsymbol{R}(\boldsymbol{u}^i)}{\partial \boldsymbol{u}}(\delta \boldsymbol{u})\right|_{i+1} > \left|\dfrac{\partial \boldsymbol{R}}{\partial \boldsymbol{u}}(\delta \boldsymbol{u})\right|_i$ **then**
7 $\quad \boldsymbol{u}^{i+1} = \boldsymbol{u} - \alpha \delta \boldsymbol{u}^i$
8 $\quad \alpha = 0.5 \times \alpha$
9 $\quad$ go to line 4
10 **else**
11 $\quad$ continue
12 **end**
13 **if** $\delta \boldsymbol{u}$ *is within an acceptable tolerance* **then**
14 $\quad$ stop
15 **else**
16 $\quad$ increase iteration counter : $i = i + 1$
17 $\quad$ update $\boldsymbol{u}^i$
18 **end**
19 repeat from step 1

The algorithm essentially adjusts α using the function $0.5^n\alpha$ where n is the number of times damping is required. If damping is not required the algorithm remains the same as the standard Newton-Raphson scheme. Alternative modifications to the Newton-Raphson scheme other than the line search method may be employed: see [34] for more detail.

4.2 Implementation of the Finite Element Method

In this work the deal.ii (Differential Equation Analysis Library) finite element library was used for implementation [37]. This is an open source C++ library which uses object-oriented programming to implement the finite element method. The library comprises various tools such as mesh generation, finite elements, quadrature rules, linear algebra tools, mesh refinement tools and many others which are essential for implementing the finite element method. The library also interfaces with other linear algebra packages such as PETSC, Trilinos and UMFPACK for additional functionality. Deal.ii code allows the

user to modify it at any level and has a large repository of documentation available.

In deal.ii, a finite element problem is treated as an object with various methods and objects as its components. The methods include functions that perform tasks such as assembling the tangent matrix, computing the residual vector, and applying the boundary conditions. The objects include the shape functions and the mesh. Modifying deal.ii finite element code is made easier as the code is written using inheritance. The shape functions for various element types are based on a base element which allows the element type to be changed without changing the majority of the code. Since the discontinuous elements are already available in the library, such modifications are not required but may be useful to other users.

The algorithm for assembling the tangent matrix in deal.ii is as follows:

Algorithm 3: Assembly of the tangent matrix

```
1  Initialise element data and containers;
2  for each element do
3      extract old solution values;
4      for quadrature point in the element do
5          get shape function values, that is pre-compute w, q and σ ;
6          for degree of freedom do
7              compute internal contribution of the element all terms in ∫_Ωe from
               equations (4.5), (4.6) and (4.7) ;
8          end
9      end
10     distribute local contributions to global tangent;
11     use constraint matrix to enforce the velocity boundary conditions based on
       equation (6.1) ;
12     for face on the element do
13         if face is on boundary then
14             weakly enforce discontinuous Galerkin boundary conditions;
15         else
16             compute discontinuous Galerkin edge term contributions (see algorithm
               4);
17         end
18     end
19     distribute local discontinuous Galerkin contributions to global tangent;
20 end
```

The edge terms for the Discontinuous Galerkin method are computed using the following algorithm:

Algorithm 4: Computing the contribution of DG-Upwinding boundary terms

```
1  Initialise face data and containers
2  extract old solution values
3  for quadrature point in the element do
4      get shape function values
5      for degree of freedom do
6          if face is upwind, i.e k · n > 0 then
7              compute upwind contributions using upwind test functions the terms on
               ∫_{Γe+} in equation (4.7)
8          else
9              compute downwind contributions using downwind test functions the
               terms on ∫_{Γe+} in equation (4.7)
10         end
11     end
12 end
```

4.2.1 Adaptive Mesh Refinement

Often in finite element methods a very fine mesh is required to obtain the desired accuracy. However finer meshes result in higher computational costs. Adaptive mesh refinement addresses this by increasing the accuracy of the problem while keeping the problem relatively small. The technique refines the mesh in regions where the change in the solution field is more pronounced, i.e. where the second derivative is high [38]. The solution however is not known beforehand so adaptive meshes are generated iteratively. The basic algorithm for adaptive mesh refinement is as outlined below:

Algorithm 5: Procedure for Adaptive Mesh Refinement

1 solve the problem on an initially coarse mesh
2 compute the error indicator for every element based on the solution
3 **if** *the solution accuracy is within an acceptable tolerance* **then**
4 | stop
5 **else**
6 | continue
7 **end**
8 mark the elements with an unacceptably large error indicator and refine them
9 repeat from line 2

For triangular elements mesh refinement is relatively simple. Quadrilateral elements however present a problem as refining the mesh locally may result in hanging nodes, as illustrated in Figure 4.1.

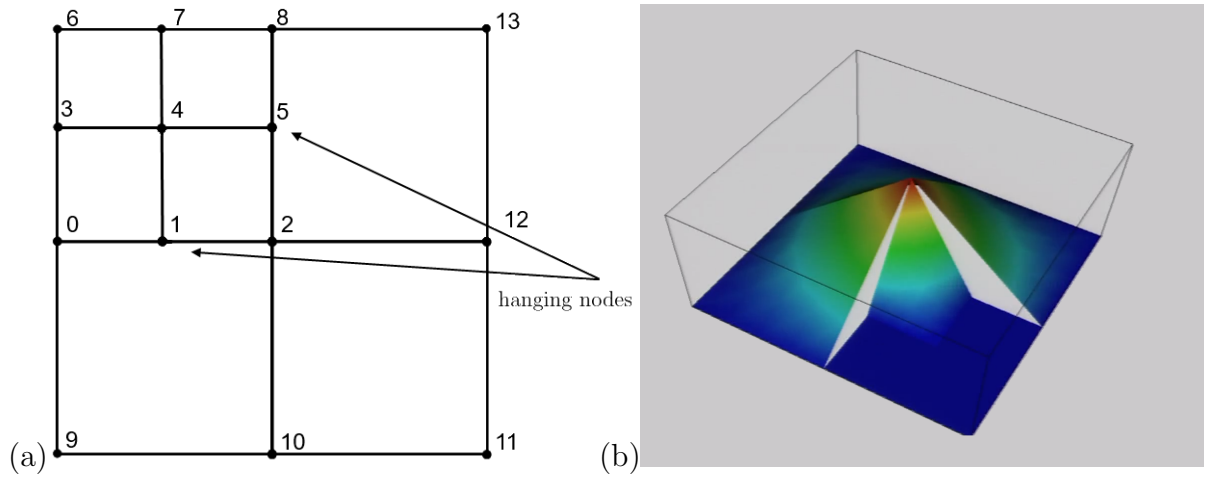

Figure 4.1: (a) Refined mesh with hanging nodes 1 and 5. (b) Discontinuous shape function resulting from hanging node.

The setup in 4.1 results in discontinuous shape functions, however the functions in W^h are required to be continuous. To ensure that the trial and test functions are globally continuous, additional constraints are placed on the functions associated with the hanging nodes. The constraints require that the subset of the degrees of freedom associated with the hanging nodes can be written as linear combinations of other degrees of freedom. For example the values at hanging nodes 1 and 5 are written as

$$d_1 = \frac{1}{2}(d_0 + d_2), \qquad d_5 = \frac{1}{2}(d_2 + d_8).$$

In the context of deal.ii, constraints are handled by the `make_hanging_node_constraints` which are then added to the object from the `ConstraintMatrix` class. For more detail on dealing with constraints see [39].

4.2.2 Parallel Computations

For relatively large computational problems it is necessary to perform computations in parallel. There are two forms of parallel computing, viz. shared memory and distributed computing. Shared memory involves making all the information about the mesh and variable storage available to multiple processors performing operations on them. This is implemented using classes in the `Threads` namespace in deal.ii. The class ensures that only one local contribution to the system is written into the the memory at a time to avoid conflict.

Distributed memory involves splitting the mesh and access to variable storage across multiple processors. Each processor only has access to a part of the system and its interface to its neighbouring elements owned by other processors. This called locally relevant data (cells and degrees of freedom). In this work a distributed memory approach is used in order to gain access to the Amesos SuperLU DIST solver from Trilinos used in [3]. The benefits of this solver are that it is a parallel direct solver which handles larger problems faster without the need for preconditioning. An additional bonus of using this method in deal.ii is that the changes in the code from a serial code to a distributed memory approach are minimal.

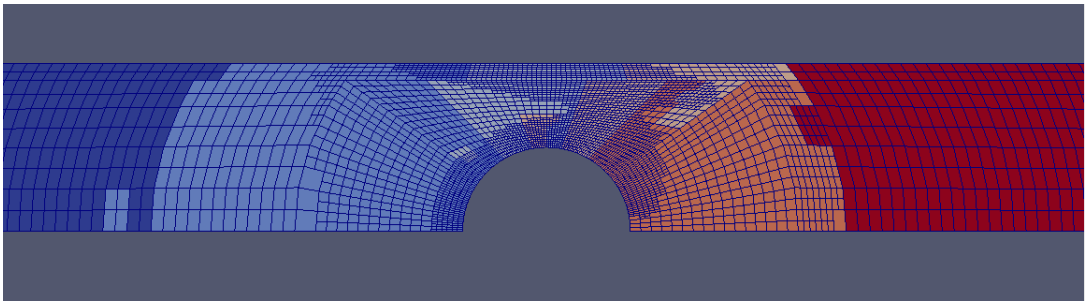

Figure 4.2: Mesh subdomains distributed to processors.

Chapter 5

Benchmarks

The validity of the model used in this work and its implementation in an open-source environment are tested using a benchmark problem viz, flow past a confined cylinder. The history of the problem in the context of numerical solutions for the Oldroyd-B fluid is reviewed in the opening section of this chapter. A description of the problem used in this work is then presented, followed by the results obtained.

The later sections of the chapter deal with the mesh convergence study conducted, and the effect of the Weissenberg number on the various solution fields.

5.1 Flow Past a Cylinder

Two-dimensional flow past a cylinder is used as a standard benchmark test for Newtonian fluids as well as various non-Newtonian fluids, including the Oldroyd-B fluid [40, 11, 41, 42, 43]. Flow past a cylinder or arrays of cylinders has industrial applications such as in heating and cooling systems, food processing, fibre coating and oil recovery [40, 11].

The geometry of the problem has no singularities, but the challenge lies in predicting the sharp stress boundary layers that arise around the obstruction and along the axis of symmetry in the wake of the obstruction [40].

The majority of studies have focused on obtaining solutions for high Weissenberg numbers with different numerical methods. In these studies most schemes fail to converge at Weissenberg numbers of 0.7/0.8. The problem has also been shown to be mesh-sensitive with increasing Weissenberg number. Though some solutions have been obtained for higher Weissenberg numbers, there is still uncertainty about the accuracy of the solutions obtained [42]. Despite this there is agreement to an extent on the expected behaviour in this setup, for this work the expected behaviour and plots obtained in literature will be

used as a measure of success.

In the literature various methods have been used to test the Oldroyd-B fluid using this benchmark. A finite element approach has been carried out by Kim et al. [9] using DEVSS-F/SUPG. Convergence could only be obtained for Weissenberg numbers up to 0.7. In [10] a Local Projection Stabilization (LPS) method was used to allow the interpolation order of the velocity and stress fields to be the same; here results for Weissenberg numbers up to 2.25 were published. Fan et al. [2] used a combination of EVSS, DEVSS, MXI with h-p finite elements and an SUPG method to solve the constitutive equation. A Galerkin Least Squares (GLS) method was also employed by Coronado et al. in [11] and as a log-conformation formulation with DEVSS-TG/SUPG in [41], while a fully implicit log-conformation approach based on the analytical structure of the constitutive equation was used in [44], allowing for faster Newton-Raphson schemes. An extended finite element method (XFEM) has been employed in [12]. Other work using finite elements includes studies in [42, 45].

A finite volume study has been carried out in [40]; here a log-conformation formulation was employed. In [46] high resolution MINMOD and SMART were used. A finite volume method coupled with DAVSSS-ω was used in [47]; the results presented here reached Weissenberg numbers up to 1.8. Work on the 3D equivalent of the benchmark was carried out using an upwind least squares semi-staggered dilatation-free finite volume method in [48].

Spectral element methods were employed by Kynch and Phillips [49] where a DEVSS-G/DG formulation was used for stabilization; convergence was limited to We = 0.7. Spectral/hp elements were used in [50], while a LUST (locally up-winded spectral technique) was used in [51] where the maximum convergent Weissenberg number was 0.8. An analysis on the performance of SPH (smoothed particle hydrodynamincs) in flow past an array of cylinders has been carried out in [52].

Experimental work on flow past a cylinder or arrays of cylinders using polymer solutions was conducted in [53, 54]. A detailed study of the benchmark can also be found in Chapters 9 and 10 of [16].

5.2 Benchmark Problem Statement

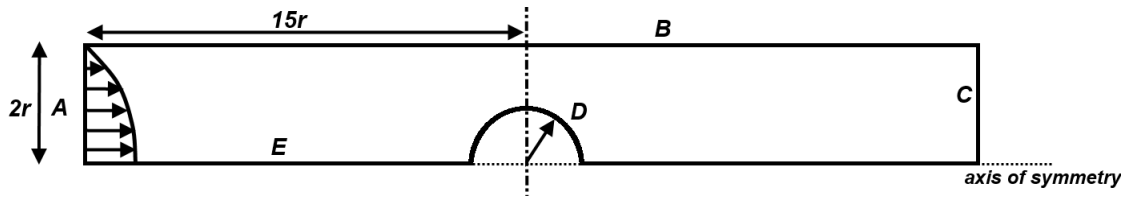

Figure 5.1: Geometry of channel with cylindrical obstruction

The benchmark problem considers flow of a fluid in a channel with a cylindrical obstruction. Since the cylinder is symmetrically placed in the channel only half of the problem is considered, as shown in Figure 5.1. The channel is rectangular with a width $4r$, where r is the radius of the symmetrically placed cylindrical obstruction. The channel half-length $15r$ is sufficiently long for the flow to fully develop, ensuring that the boundary conditions do not affect the behaviour at the obstruction.

The inlet velocity (along inlet A) is obtained from the analytical solution for Poiseuille flow of an Oldroyd-B fluid, see Appendix A of [6]. The extra stress inlet is weakly set to zero for all components. The effect of imposing the analytical solution obtained from Poiseuille flow was found to be negligible since the flow will develop to that state in the channel, hence the zero boundary condition was chosen for convenience. No-slip boundary conditions are used for the channel wall (B) and the cylindrical obstruction (D). On the axis of symmetry (E) the boundary conditions are set to,

$$\frac{\partial \boldsymbol{u}}{\partial y} = \frac{\partial \boldsymbol{\tau}}{\partial y} = \boldsymbol{u} \cdot \boldsymbol{n} = 0.$$

The parameters used for this study are $Re = 0.1$, $\beta = 0.59$ and Weissenberg numbers ranging from 0.1 to 0.6, for which the algorithm was found to be convergent in the literature, with 0.7 being the limiting Weissenberg number for the stability. A steady state scheme is run for the problem, as opposed to a transient solution which is time-stepped to equilibrium as in [6, 8]. Such a scheme showed the same results as the steady scheme for $\mathrm{We} = 0.6$, so to save computational cost the remainder of the problem was computed using a steady scheme. The convergence criterion was set to a residual tolerance of 1×10^{-6}; results at lower tolerances 1×10^{-12} were found to have a negligible effect on the solution profiles.

5.3 Solution Profiles

Solution profiles were obtained for Q_0 and Q_1 discontinuous elements used for the extra stress fields. Another factor taken into account is the computational cost of working at higher Weissenberg numbers. The algorithm employed showed that computational time increases with Weissenberg number and the use of Q_1 elements further increases this.

The solution profiles for the three fields (velocity, pressure, polymeric stress) at We = 0.3 in the vicinity of the obstruction are shown in Figure 5.2. The velocity profile was found to be very close to that of a Newtonian fluid in the same configuration with the flow past the cylinder being nearly double the flow in the open channel. The components of the extra stress tensor show similar trends to those shown in [2] [6] [12]. The τ_{xx} component shows tensile stretching of the fluid at the peak of the cylinder as well as on the channel wall directly above the cylinder. Another rise in the tensile component is seen in the wake of the cylinder. The τ_{xy} component shows a rise in the shear along the left cylinder wall and a subsequent fall in the stress on the right cylinder wall. The vertical component τ_{yy} reaches a maximum before the cylinder peak with additional stretching on the opposite side. In the zero velocity region downstream of the cylinder there is a stress free zone with the τ_{yy} component showing the steepest gradient close to this zone.

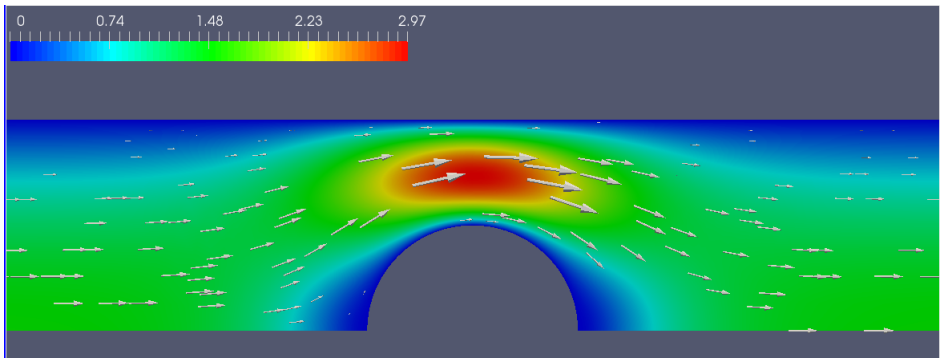

(a) *velocity profile*

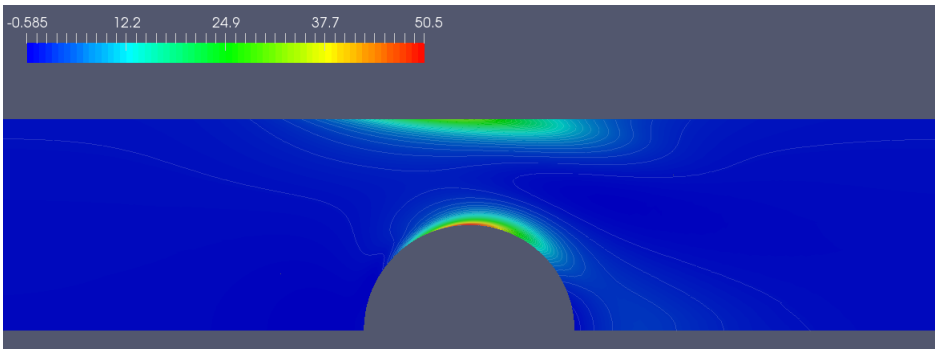

(b) τ_{xx} *profile*

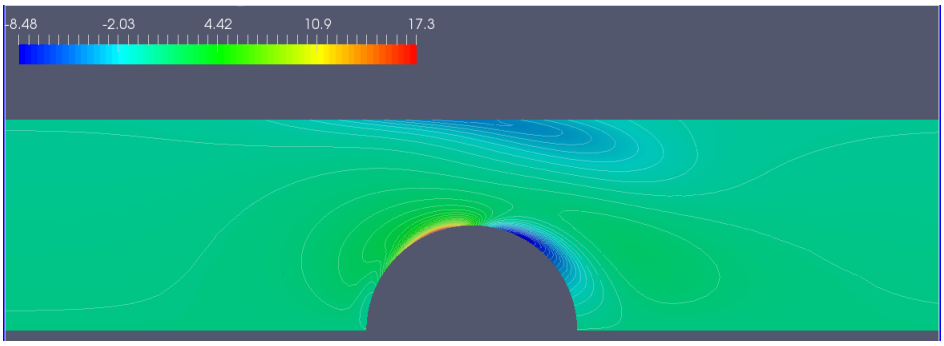

(c) τ_{xy} *profile*

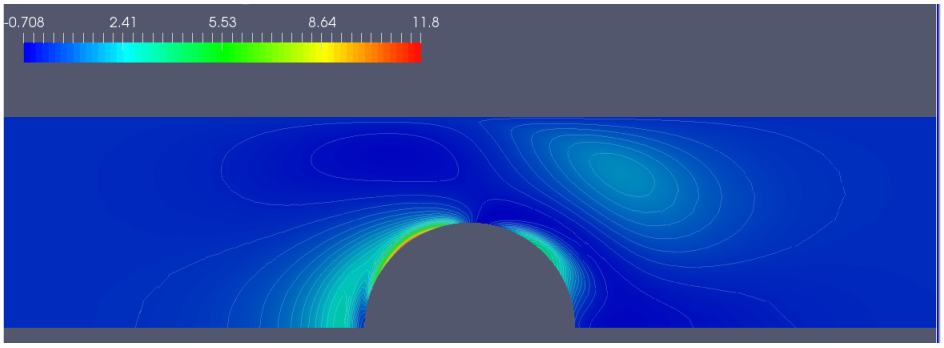

(d) τ_{yy} *profile*

Figure 5.2: Steady state solution for the Oldroyd-B fluid (We = 0.3)

5.4 Mesh Convergence

A convergence study was done for at We = 0.3 using meshes M0-M4 shown in Figure 5.3, with M3 and M4 only showing the region closest to the obstruction. The meshes M2 to M4 were obtained by adaptively refining in the region of highest activity based on solutions obtained in solutions from coarser meshes, as opposed to a global refinement employed from M0 to M1.

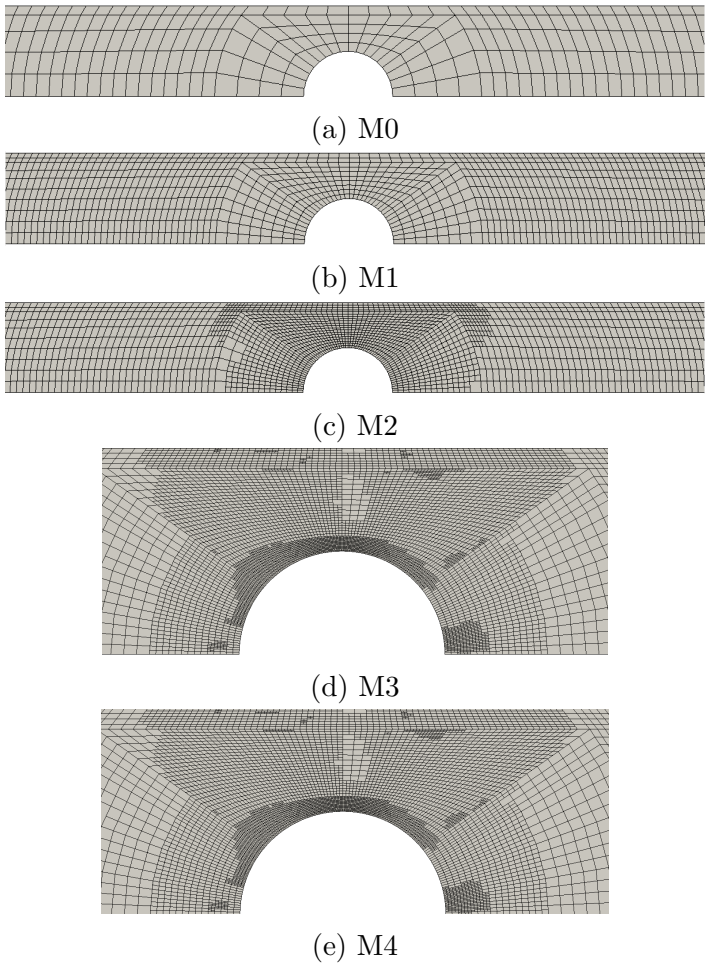

(a) M0

(b) M1

(c) M2

(d) M3

(e) M4

Figure 5.3: Benchmark problem mesh for increasing mesh refinement M0-M4

The mesh refinement is concentrated in this region as it is the region with the highest activity. A summary of the properties of the meshes is shown in the following table.

Mesh	Number of Elements	Mesh Parameter h	Total Degrees of Freedom
M0	502	0.208	2008
M1	2008	0.0983	8230
M2	3214	0.0478	12856
M3	5143	0.0235	20572
M4	8230	0.0117	32590

Table 5.1: Summary of mesh properties for benchmark problem

In Table 5.1, h is the characteristic length of the smallest element in the mesh. The convergence trend obtained in Figures 5.4 and 5.5 was very similar to those obtained in [6, 12] for a Weissenberg number of 0.3.

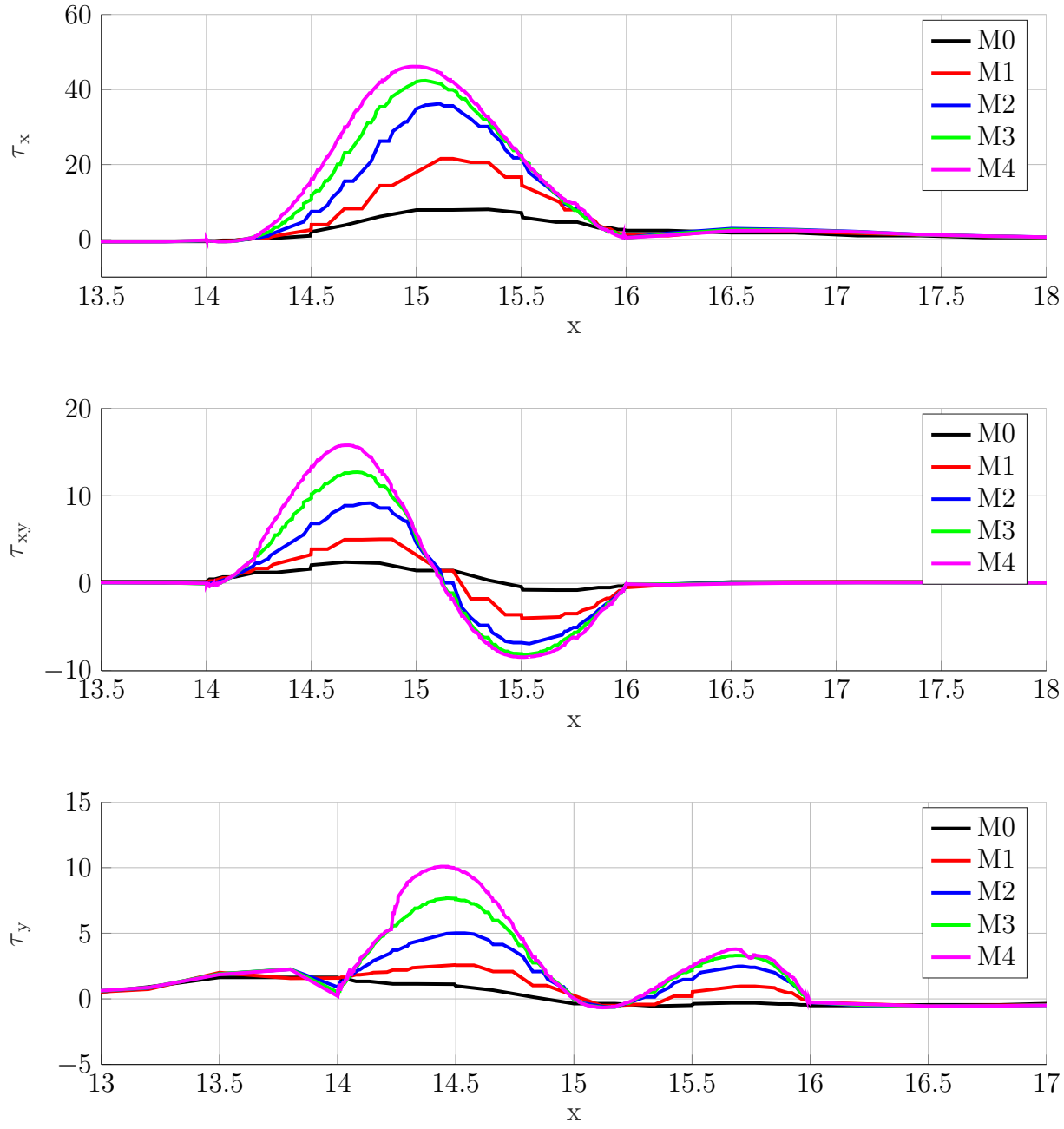

Figure 5.4: Extra stress components around the cylinder wall for varying refinement levels for Q_0 elements

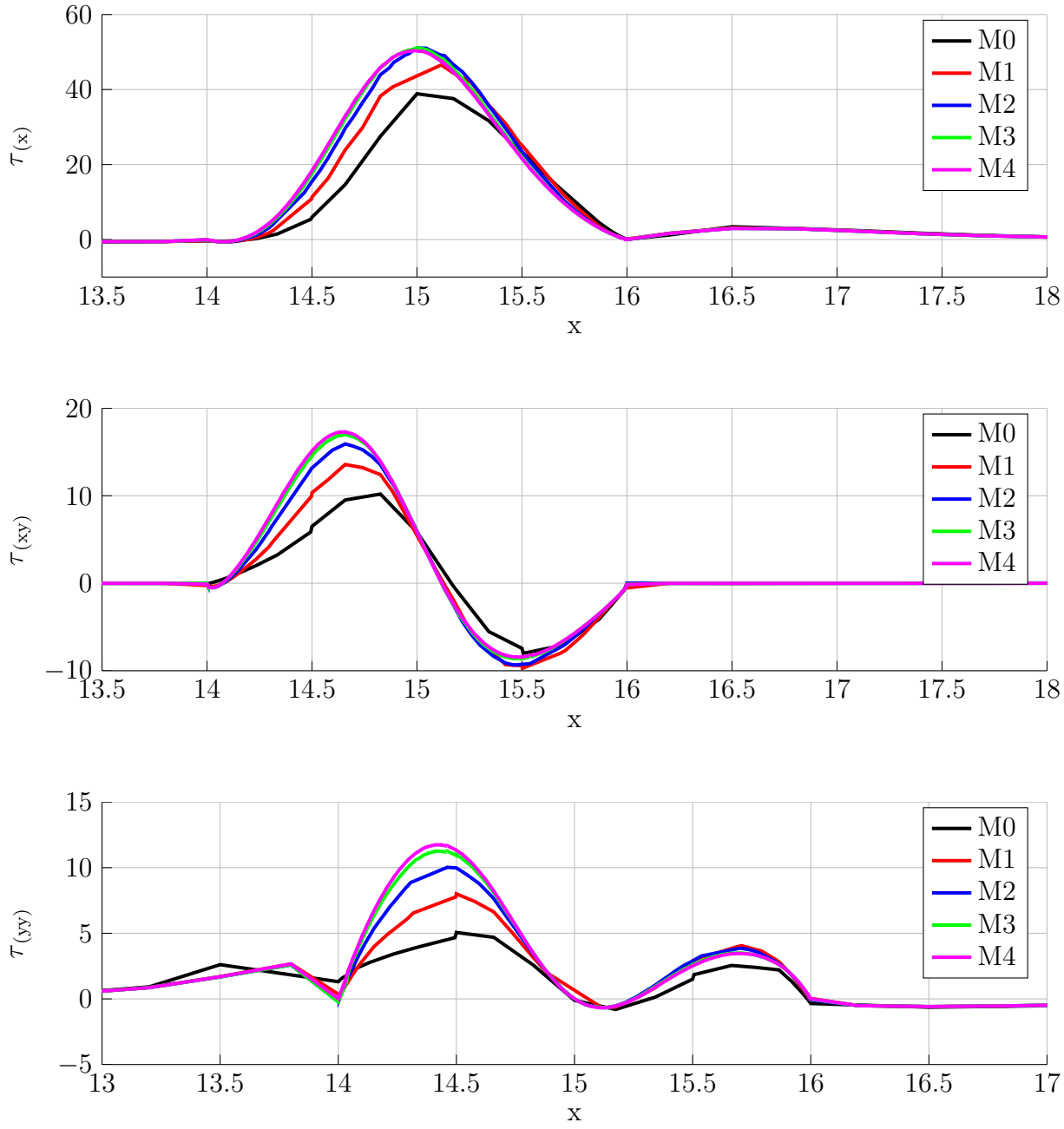

Figure 5.5: Extra stress components around the cylinder wall for varying refinement levels for Q_1 elements

The study showed that Q_1 elements predict the high stress gradients around the cylinder well, while Q_0 elements under-predict the peak extra stress values. This is even more apparent in coarser meshes using Q_0 elements. The region of detachment in the extra stress component τ_{yy} showed the greatest mesh sensitivity, as shown in [6].

The velocity and pressure fields show greater accuracy at lower refinement levels. This is expected as the contribution of the extra stress to the momentum equation has a smaller impact on the velocity profile than the flow field's impact on the constitutive equation for the polymeric stress.

5.5 Effect of Weissenberg Number

The velocity and pressure fields show little variation with increasing We, while the extra stress shows greater variation. The change of the direct extra stress fields with increasing Weissenberg number is shown in the following Figure.

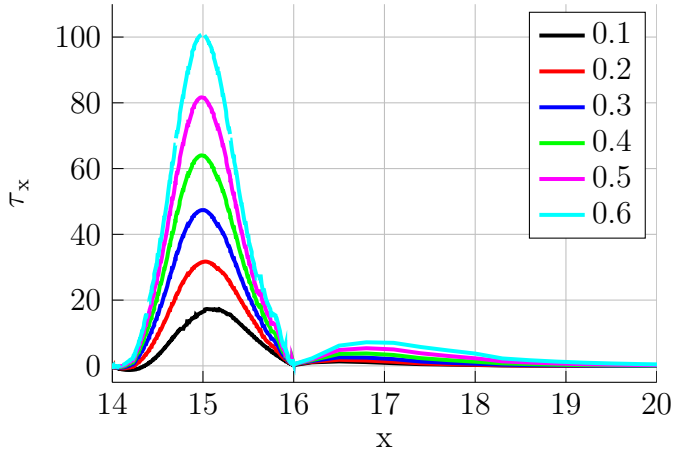

(a) Q0 elements

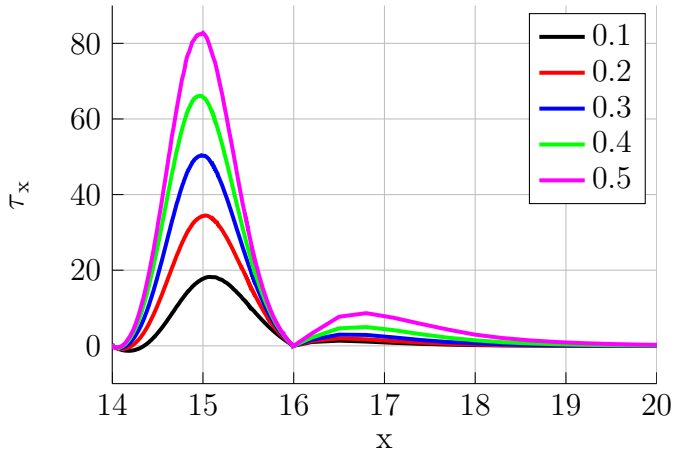

(b) Q1 elements

Figure 5.6: Direct polymeric stress for increasing Weissenberg Number.

For Q_1 the algorithm failed to converge at We = 0.6. The results in Figure 5.6 closely follow those presented in [6, 12] for Weissenberg numbers between 0.1 and 0.4. The results for We = 0.5 and 0.6 have higher peaks and are similar to those obtained in [2, 40, 42]. The extra stress shows steeper boundary layers with increasing Weissenberg numbers along the cylinder. The behaviour at the wake of the cylinder for We = 0.5 and 0.6 differs from that in the literature with lower peak values in the wake. For these Weissenberg numbers the algorithm is not as accurate, this is likely because we are approaching the unstable We for this scheme. Further adjustments to the algorithm such as pressure projection methods may result in more accurate results for this range.

5.6 Dimensionless Drag

The dimensionless drag is frequently used as a measure of accuracy of a solution method. This value however should not be used as the only validation for the accuracy of the solution method because it is an integral quantity which may cancel out errors and is not sensitive to the local variation of extra stress [9]. For the symmetric problem the dimensionless drag over the cylinder (D) in Figure 5.1 is calculated as

$$F_D = -2 \int_D \boldsymbol{e}_x \cdot (-p\boldsymbol{I} + \beta(\boldsymbol{\nabla u} + \boldsymbol{\nabla u}^T) + \boldsymbol{\tau}) \cdot \boldsymbol{n} \, \mathrm{d}\Gamma. \tag{5.1}$$

Dimensionless drag values were obtained for both Q_0 and Q_1 elements at mesh refinement M2 for consistent comparison with the literature. A comparison of the dimensionless drag values obtained for varying We with values from literature is presented in Table 5.2.

We	M2 Q_0	M2 Q_1	Donev [6]	Fan [2]	Kim [9]	Hulsen [42]	Claus [50]
0.1	129.297	130.311	130.558	130.36	130.359	130.363	130.364
0.2	125.546	126.511	126.629	126.62	126.622	126.626	126.626
0.3	122.371	123.018	123.089	123.19	123.188	123.193	123.192
0.4	120.256	120.396	120.393	120.59	120.589	120.596	120.593
0.5	119.237	118.660	118.656	118.83	118.824	118.836	118.826

Table 5.2: Table of dimensionless drag F_D compared to literature.

The values obtained for Q_1 elements show very close correlation with values in the literature. The results show the same parabolic trend even though the full profile is not seen in this work as the minimum of the parabola is not visible for the range of We used. The dimensionless drag values are only presented for Weissenburg numbers less than 0.6, where the algorithm showed the closest correlation with literature. The values obtained for Q_0 show a greater difference to those presented in literature, as observed in [6]. The trend observed in [6] for Q_0 elements is not observed here, however the Q_0 results from this work were found to be slightly closer to those from other literature than [6]. A comparison of the dimensionless drag values for Q_0 and Q_1 elements with [2, 6] is shown in Figure 5.7.

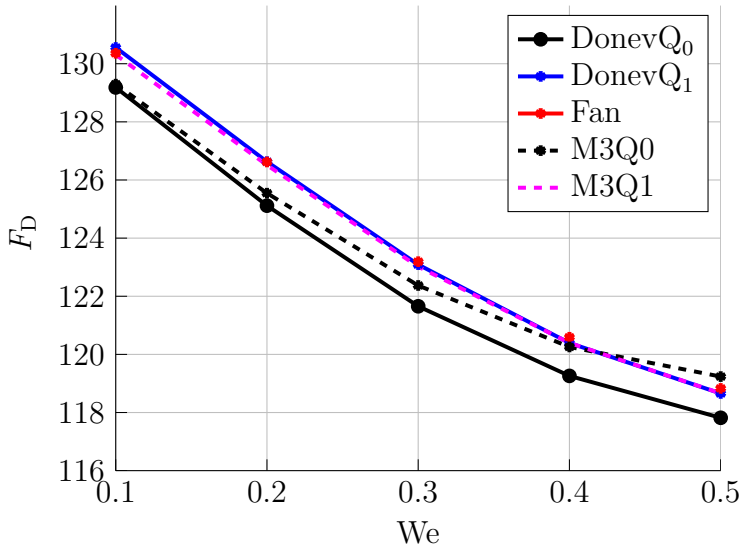

Figure 5.7: Dimensionless drag profile for Q_0 and Q_1 elements compared to [1, 2].

Based on the results obtained, it is seen that mesh M3, with $h = 0.0235$, is at a sufficiently fine refinement level for obtaining accurate results for the benchmark problem. The results also show that though Q_0^{disc} elements produce decent predictions for the behaviour of the fluid, Q_1^{disc} elements are a better choice for accurate results. The results also show the closest agreement with data from the literature for Weissenberg number up to We $= 0.4$. This in agreement with the literature as solutions obtained were more varying in literature with increasing We.

Chapter 6

Application to blood flow in a complex geometry

This chapter deals with the simulation of blood flow in a complex geometry, using the Oldroyd-B model. The context of the problem is an arteriovenous fistula (AVF), which is a form of vascular access used for haemodialysis. Detailed treatment of this problem using a Newtonian fluid can be found in [3]. The objective of this work is to explore the influence of using a non-Newtonian model that more closely resembles blood.

The properties of blood and the relevance of various fluid models in this context are reviewed in section 6.1. Then in section 6.2 the haemodynamics of the AVF are discussed. A brief review of the AVF in literature in the context of modelling is also presented.

The details of the geometry used in this work and the complex set of boundary conditions required due to the complexity of the geometry are discussed in section 6.3. The flow profile and wall shear stress results obtained by using a Newtonian fluid from this work are compared to MRI data and FSI from the literature in section 6.4.1. The remainder of the chapter is concerned with the results obtained from using a viscoelastic fluid, these results are compared for varying We and to the results from using a Newtonian fluid.

6.1 Properties of Blood

Blood is composed of a plasma and cells suspended in the plasma. The cells are erythrocytes (red blood cells), leukocytes (white blood cells) and platelets, which form about 45% of the volume. The mechanical properties of blood are largely influenced by the concentration of red blood cells which form the bulk of the particles. The membrane of red blood cells is elastic, allowing them to release and store elastic energy. Blood also exhibits shear thinning behaviour due to red blood cells forming long chains called

rouleaux. The viscosity of the blood increases when rouleaux are formed and decreases at higher shear-rates, where the rouleaux break up and align with the direction of flow [55].

Though blood is a shear thinning fluid, at shear rates greater than $100/s$ the viscocity can be treated as constant. More complex properties such as thixotropy, platelet activation and clotting are considered negligible when considering reasonably healthy blood flow [19, 56].

In the literature, blood in large arteries is generally modelled as a Newtonian fluid. Newtonian models for blood have provided good approximations in many flow regimes (see [57] for experimental validation). Much of the focus has been placed on the study of shear-rate dependent models for blood (see for example, [58, 59, 60, 19, 61, 62]) and coupled FSI problems [63, 64, 3, 65, 13] where the vessel walls are assumed deformable.

The use of viscoelastic models to model blood flow has also received some attention in the literature. In [5] a generalised Oldroyd-B model was used to model blood, and was validated experimentally using porcine blood. The results using this model were more accurate compared to a Newtonian model, and the former was subsequently used by other authors [66, 60, 67]. A viscoelastic model based on a thermodynamic framework was developed in [68]; this model showed good correlation with experiments conducted in [69]. A FENE model was used in [70], for modelling shear-thinning in small blood vessels. In [1], a generalised Oldroyd-B model was used for modelling flow in arterial stenosis, which is an abnormal narrowing of the blood vessels due to an obstruction formed by fat deposits and plaque build up in the vessel walls [57].

6.2 The arteriovenous fistula (AVF)

An arteriovenous fistula is a form of vascular access formed by connecting an artery and a vein. Arteriovenous fistulae (AVF) are used in hemodialysis, which is required by most patients with late stage renal disease. For this treatment blood is extracted from the body into a filter through a tube. The process requires blood flow rates above 300 ml/min [71].

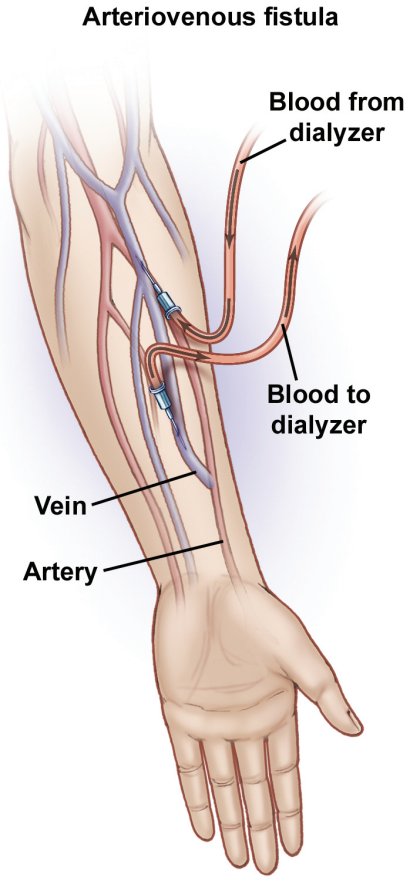

Figure 6.1: An illustartion of arteriovenous fistula *(http://westcoastvascular.com/dialysis-access-center/av-access)* where the fistula is used to obtain higher blood flow rates than normal during dialysis.

The haemodynamics in the vein are altered in an AVF; the flow changes from steady to pulsatile, the pressure increases from an average of 20 $mmHG$ to values between 60 $mmHG$ and 120 $mmHG$, and the wall shear stresses are much higher [72, 73]. The most common reason for AVF failing in a patient is thrombosis, the formation of a blood clot. Thrombosis in vascular access is preceded by stenosis which is a narrowing of blood vessels.

Compuational fluid dynamics simulations were carried out in [72, 74, 75, 76, 77] on the AVF and exhibited flow features such as recirculation, stagnation and separation. Shear thinning fluids were used for AVF modelling in [78, 79]. Fluid stucture interaction studies on the AVF in [71] showed that the CFD studies using rigid wall assumptions overestimated the vessel wall shear stresses. A finite element code was coupled to a commercial fluid solver in [80] to simulate blood flow within an idealised model of the AVF using a Carreau model. In [13] an FSI model was developed by combining a finite volume method blood flow model, using ANSYS® Fluent® and a finite element method vessels wall model with ANSYS® Mechanical™. In [3] a monolithic finite element method approach was

used to solve the FSI system for an AVF.

In this work the aim is to compare results using a Newtonian fluid with those for viscoelastic fluids for blood flow in the AVF. It appears that such a comparison is not available in the current literature. Rigid wall assumptions will be used as the use of FSI models falls outside the scope of this work.

6.3 Geometry

The geometry used for this work was obtained from [3], where velocity encoded MRI data was used to obtain a patient specific model for a fistula using ANSA meshing software. More detail on the data acquisition process can be found in [3].

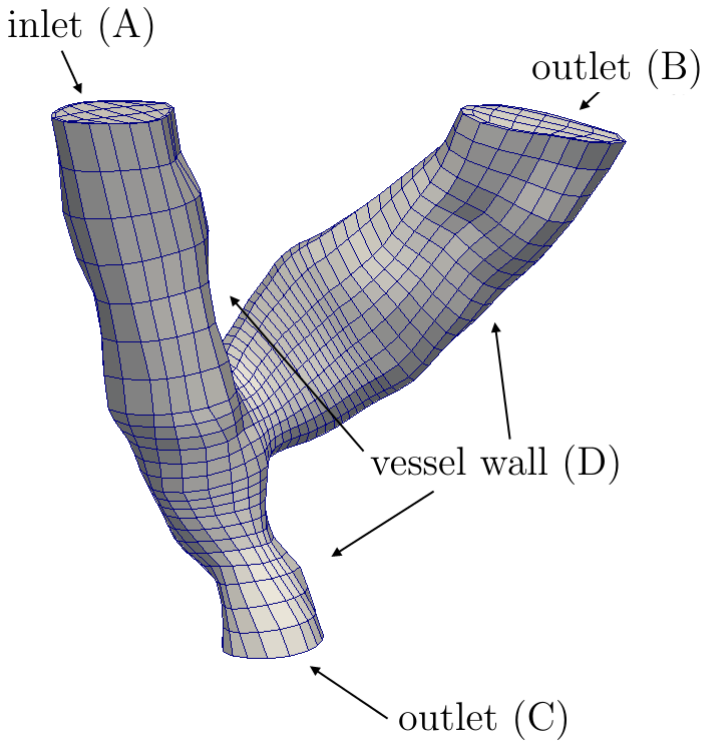

Figure 6.2: Geometry of the arteriovenous fistula processed from MRI data, the artery is from inlet (A) to outlet (C) and the vein is joined towards outlet (B)

The geometry of the AVF is shown in Figure 6.2: the AVF has an inlet at A and two outlets B and C. A no-slip boundary condition is applied to the wall D.

6.3.1 Inlet flow

The velocity for the inlet flow was obtained from velocity encoded MRI scans. The data in [3] showed that the velocity profile at the inlet was approximately paraboloidal. Therefore that maximum velocity was used to construct a paraboloidal inlet velocity.

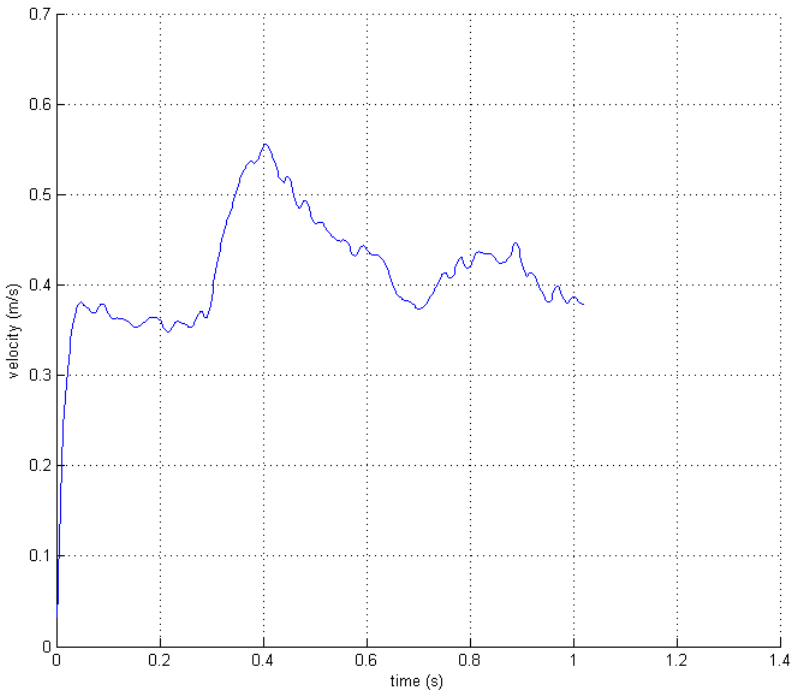

Figure 6.3: Time history of the maximum velocity at the fistula inlet from velocity encoded MRI scans

Figure 6.3 shows the maximum velocity at the inlet over time, scaled to enable comparison to the MRI data as was done in [3]. The paraboloid is approximated by the equation

$$u_{max} = u_{normal} = u_z = \left(\frac{(x + 0.1865)^2}{0.00405^2} + \frac{(y - 0.0137)^2}{0.0048^2} \right) - 1. \tag{6.1}$$

The use of equation (6.1) gives the inlet profile shown below.

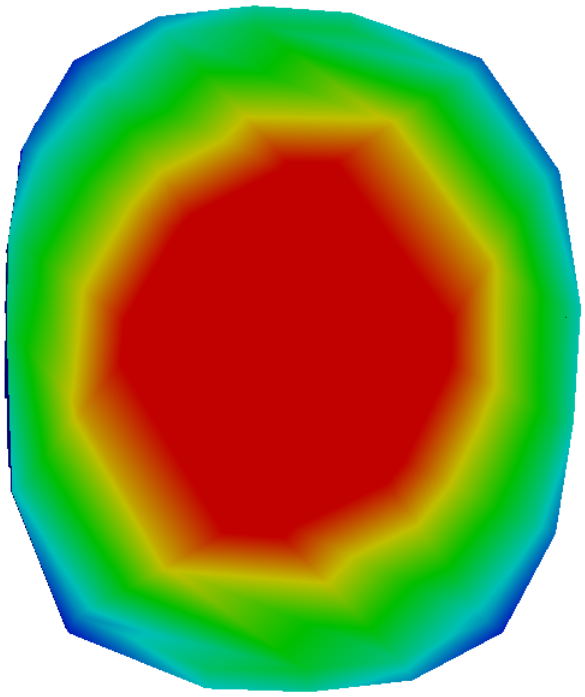

Figure 6.4: Inlet velocity profile

6.3.2 Outlet boundary conditions

When prescribing boundary conditions for blood flow, the wave propagation phenomena in the vascular system need to be taken into account. Prescribing a pressure and velocity is not applicable, as obtaining the data at the outlets is impractical and synchronization of the wave form in a manner consistent with the wave propagation is difficult. In addition to wave propagation, another physiological phenomenon in blood flow is backflow. Backflow at the outlets can give rise to numerical divergence due to the velocity profile not being specified; this is known as backflow divergence. In simulations backflow divergence is a common problem. Backflow divergence may be caused by bulk flow reversal at the outlet, localised flow reversal due to recirculation and using multi-scale models where velocity profile information is missing [81]. Artificial elongation of the outlets to ensure unidirectional flow is the simplest method to resolve backflow divergence. This method has several problems, however: it cannot be used where total flow reversal occurs, it potentially changes local haemodynamics, and adds additional computational costs [81]. Alternative methods to solve for backflow divergence were compared in [81]. The three methods used are: adding backflow stabilization terms to the weak form of the Neumann boundaries [82]; confining the outlet flow to one direction such as the normal; and using Lagrange multipliers to constrain the velocity profile to an assumed form. The backflow

stablilization method was found to be stable , inexpensive and had the least impact on the flow field [81]. In this work a variation of the backflow stabilization coupled with a resistance boundary condition is used as in [82]. The boundary condition at every outlet face is set as:

$$\boldsymbol{n}^T \tilde{\boldsymbol{\sigma}} \boldsymbol{n} + R_{out} \int_{\Gamma_{out}} \boldsymbol{u} \cdot \boldsymbol{n} \; \partial\Gamma_{out} + p_0 = 0, \tag{6.2}$$

where

$$\tilde{\boldsymbol{\sigma}} \boldsymbol{n} = -p\boldsymbol{n} + \eta \boldsymbol{D}\boldsymbol{n} - \rho(\boldsymbol{u} \cdot \boldsymbol{n})_- \boldsymbol{u}.$$

Here $\boldsymbol{u}$ is the velocity, $\boldsymbol{n}$ is the outlet normal, η is the fluid viscosity, ρ is the fluid density, R_{out} is the resistance and p_0 the pressure level of the system. The term $(\boldsymbol{u} \cdot \boldsymbol{n})_-$ is active when there is flow reversal at the boundary, otherwise it is inactive. This term denotes the negative part of $\boldsymbol{u} \cdot \boldsymbol{n}$; that is,

$$(\boldsymbol{u} \cdot \boldsymbol{n})_- = \begin{cases} \boldsymbol{u} \cdot \boldsymbol{n} & \text{if } \boldsymbol{u} \cdot \boldsymbol{n} < 0, \\ 0 & \text{if } \boldsymbol{u} \cdot \boldsymbol{n} \geq 0. \end{cases}$$

The resistance boundary condition, shown by the second term in (6.2), is a commonly applied boundary condition. This boundary condition ensures that a physiologically realistic response is obtained by using a functional relationship between the pressure and flow [82, 83]. The resistance boundary may generalised to any functional relationship between the normal-stresses and the blood flow rate as follows:

$$\boldsymbol{n}^T \boldsymbol{\sigma} \boldsymbol{n} + f(Q_{out}) = 0.$$

Here Q_{out} is the volumetric flow rate through the outlet, given by

$$Q_{out} = \int_{\Gamma_{out}} \boldsymbol{u} \cdot \boldsymbol{n} \; \partial\Gamma_{out} = 0. \tag{6.3}$$

The concept of resistance was introduced by Hales and was later related to the viscosity and flow rate by Poiseulle [83]. For steady flow in a straight tube with constant flow rate, it is defined as the resistance to flow due to viscous effects in a channel:

$$R = \frac{p_{in} - p_{out}}{Q}. \tag{6.4}$$

More complex models such as the Windkessel model, where an electrical analogue that has a resistance in a parallel arrangement with a capacitance and resistance, are used in blood flow and the AVF context [3, 13, 64]. In the Windkessel model the functional relation is given by

$$f(Q_{out}) = \int_{\Gamma_{out}} \boldsymbol{u} \cdot \boldsymbol{n} \; \partial\Gamma_{out} + \int_0^{t_{n+1}} \frac{e^{\frac{t-s}{\tau}}}{C} \; ds = 0. \tag{6.5}$$

In this work the resistance boundary condition is used in the same manner as [82], as shown in the second term of equation (6.2). The boundary conditions are imposed weakly by adding the following to the weak form of the system in chapter 3:

$$-\int_{\Gamma_{out}} \rho(\boldsymbol{u} \cdot \boldsymbol{n})_{-} \boldsymbol{u} \cdot \boldsymbol{w} \; \partial\Gamma_{out} + \left(R_{out} \int_{\Gamma_{out}} \boldsymbol{u} \cdot \boldsymbol{n} \; \partial\Gamma_{out} + p_0 \right) \left(\int_{\Gamma_{out}} \boldsymbol{w} \cdot \boldsymbol{n} \; \partial\Gamma_{out} \right) = 0. \tag{6.6}$$

The pressure level is chosen as 85 $mmHG$ as used in [82]. The resistance value at the outlets are $R_1 = 1 \times 10^4 \; kg/(m^3 s)$ and $R_2 = 1 \times 10^3 \; kg/(m^3 s)$.

In this work the dimensionless forms of the fluid equations are used, for which an additional dimensionless resistance $\tilde{R}$ is required. This is given by:

$$\tilde{R} = \frac{RL^2}{\eta},$$

where L is the characteristic length. To convert the resistance and other quantities to their dimensionless form, characteristic parameters are required. An approximation of the average diameter of the fistula is used as the characteristic length $L = 0.008m$, and the maximum inlet velocity $U = 0.555m/s$ is used as the characteristic velocity.

6.4 Results

6.4.1 Newtonian fluid

The simulations using a Newtonian fluid are carried out using the mesh shown in Figure 6.2. These simulations are done for the dimensional and dimensionless cases. The former is done in order to have a direct comparison to FSI results from [3], while the latter is done in order to determine whether the chosen dimensionless parameters are appropriate.

Flow profile (dimensional case)

The results from the dimensional Newtonian fluid are compared to the FSI results obtained in [3] and the velocity encoded MRI data from the same source. In [3], the flow profile at different points in time from the MRI data was compared to the FSI simulation results. The flow profiles obtained from a rigid wall setup in this work is similarly shown alongside the aforementioned results for two dynamic ranges, the lower dynamic range being being $0 - 0.232 m/s$ and the higher dynamic range being $0 - 0.042 m/s$. These are shown in Figures 6.5 and 6.6.

The flow profiles obtained in this work are very similar to both those from the MRI data and [3]. Low dynamic flow shown in Figure 6.5 highlights the recirculation profile, which is in the same region as the MRI data. The lack of the recirculation at the beginning of the cycle is due to the zero velocity initial conditions chosen for both the simulations.

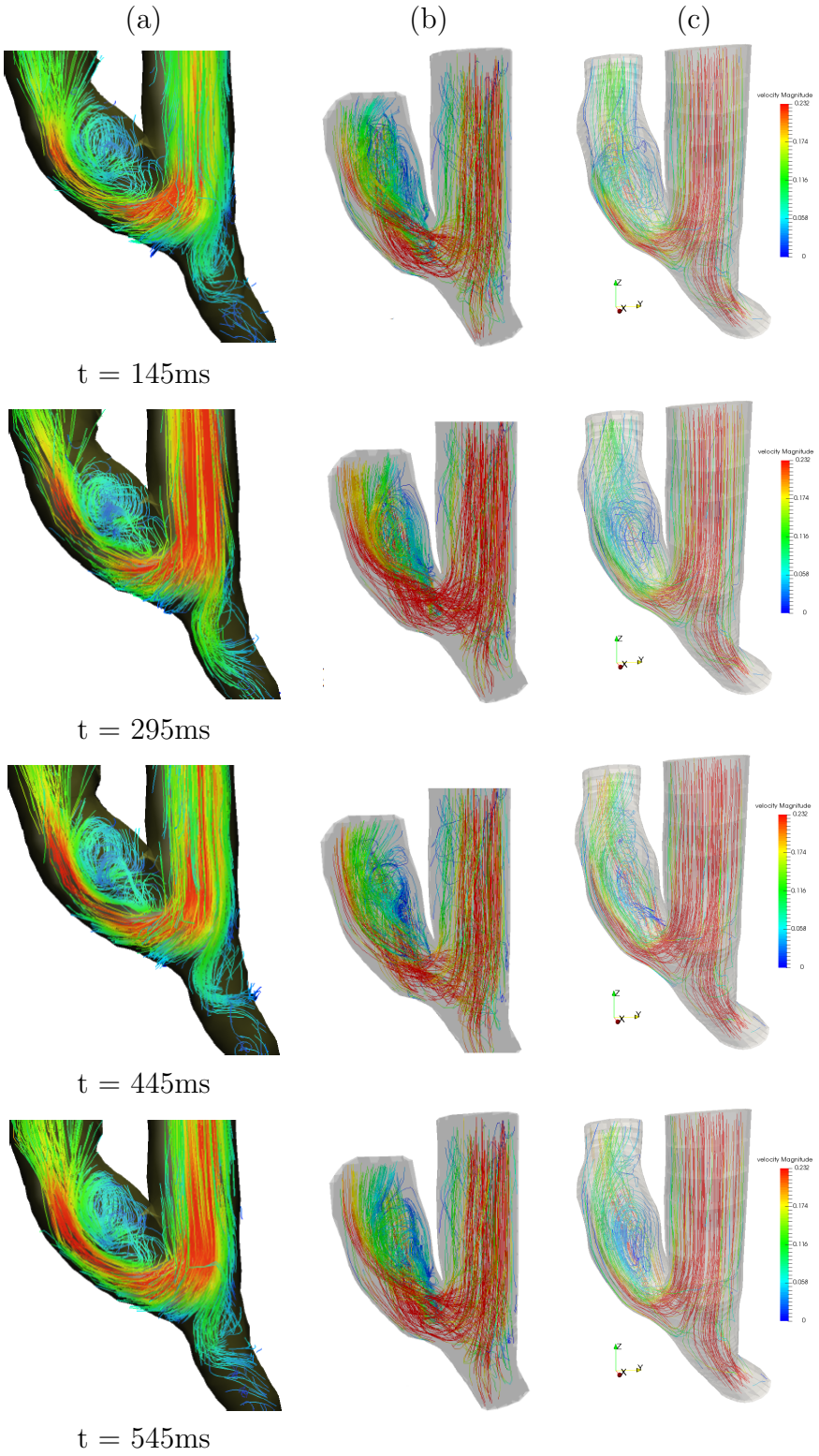

Figure 6.5: Low dynamic range velocity streamline comparison: (a) MRI data [3], (b) FSI simulations [3] (c) current work.

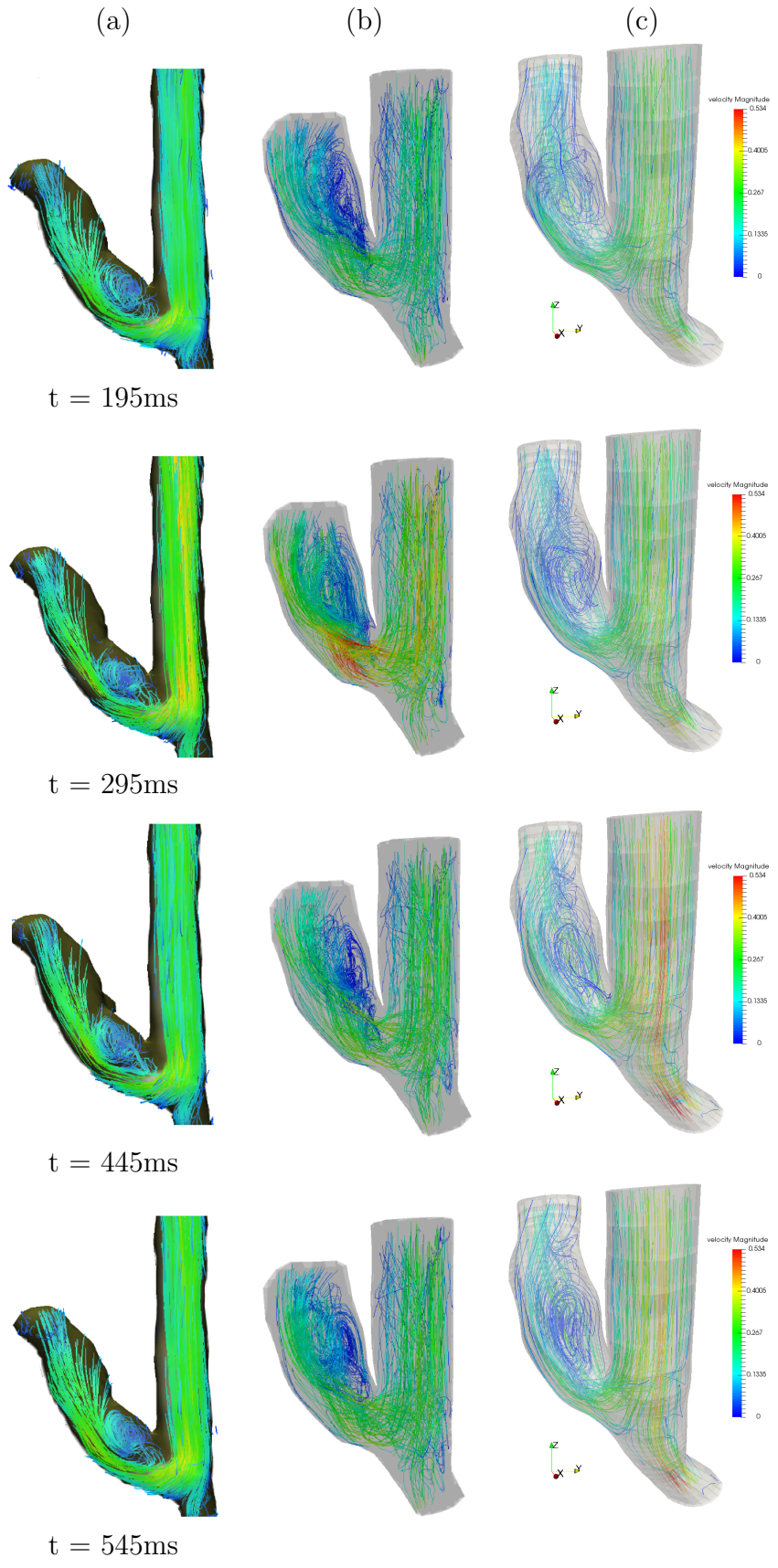

Figure 6.6: High dynamic range velocity streamline comparison: (a) MRI data [3], (b)FSI simulations [3], (c) current work.

Wall shear stress (dimensional case)

The wall shear stress (WSS) from the dimensional simulations was also computed. The WSS is defined by

$$\text{WSS} = \boldsymbol{\sigma n} - (\boldsymbol{\sigma n} \cdot \boldsymbol{n})\boldsymbol{n}. \tag{6.7}$$

It is important to compute the WSS because, the maximum WSS in vascular access is much higher than the normal physiological WSS in veins and large arteries. The WSS obtained in this work is compared to that in [3] at the peak systole in Figure 6.7.

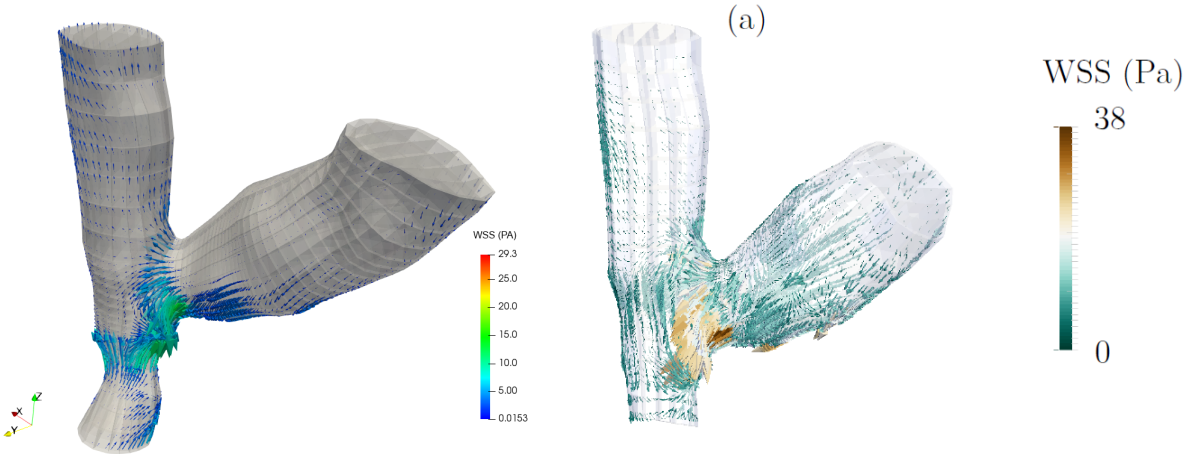

Figure 6.7: WSS comparison, (a) rigid wall simulations (b) FSI simulations [3].

In this work the maximum WSS obtained was close to 30Pa. This value is lower than the 38Pa obtained in [3]. The difference can be attributed to the difference in the outflow boundary conditions. The choice of resistance boundary conditions resulted in higher pressure values in the fistula than the Windkessel boundary condition used in [3, 13] resulting in lower WSS values since the pressure had a negative contribution in the WSS equation (6.7). Additionally, for the rigid wall setup the WSS around the base of the junction is closer in magnitude to the maximum value. This is not observed in the FSI results obtained in [3]. This is likely due to the wall compliance, which results in a slightly increased area outer wall in the region rather than the stress build-up for the case of a rigid wall.

Newtonian fluid (dimensionless case)

Before running simulations using the Oldroyd-B fluid, it is necessary to run simulations using a dimensionless Newtonian fluid. This helps with checking on whether the choice of dimensionless parameters is appropriate for the flow regime of the problem. The resulting dimensionless parameters used in the Newtonian fluid are also used for the dimensionless Oldroyd-B fluid simulations. The flow fields shown in Figure 6.8-6.9 and WSS in Figure 6.10 for the dimensionless fluid were very similar to those obtained for the dimensional setup, indicating that the parameters are appropriate for this problem.

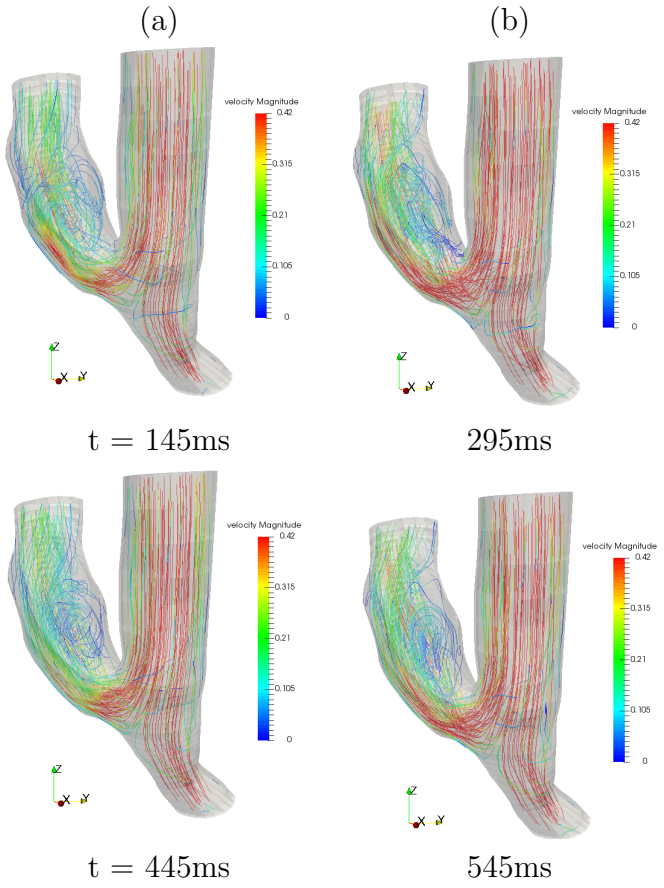

Figure 6.8: Velocity streamlines for dimensionless Newtonian fluid for low dynamic range

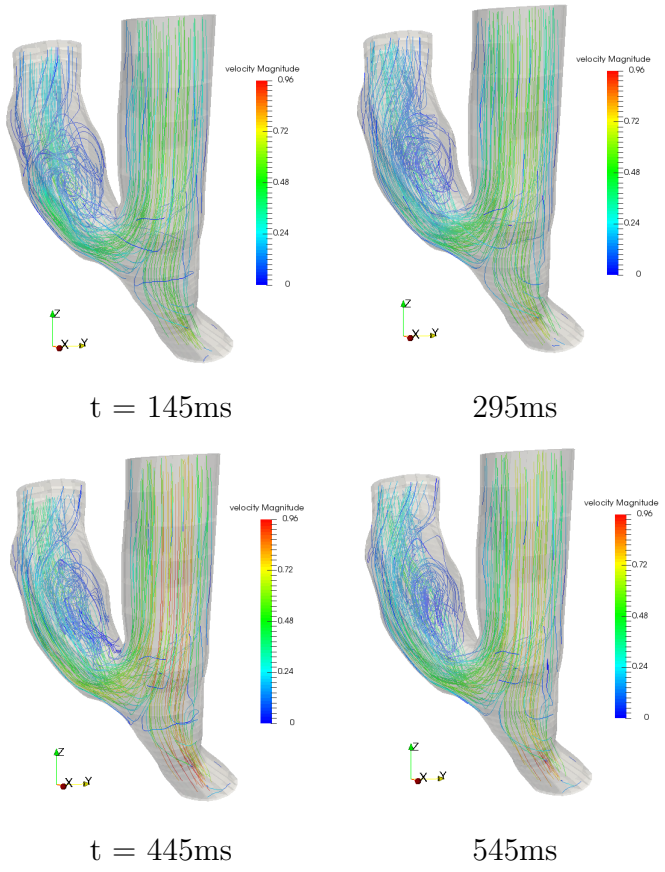

Figure 6.9: Velocity streamlines for dimensionless Newtonian fluid for high dynamic range

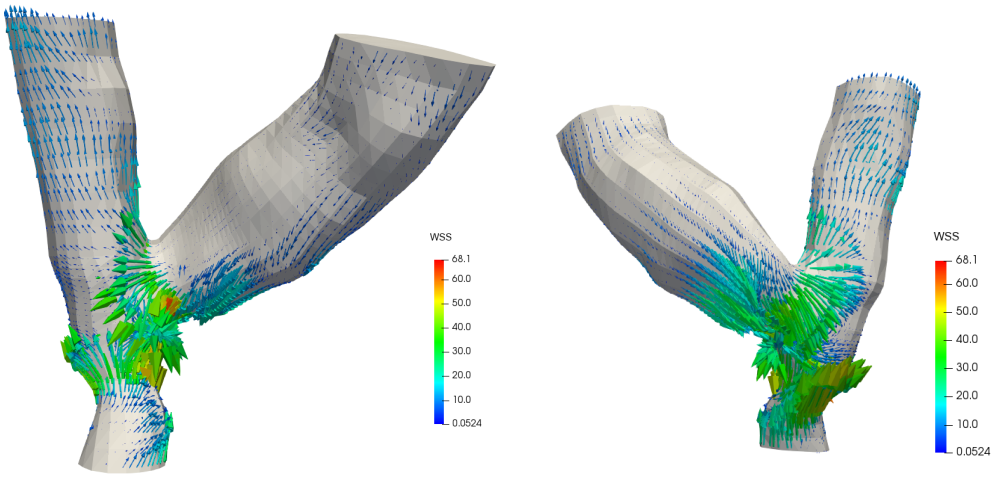

Figure 6.10: Dimensionless WSS, (a) front view and (b) back view.

6.4.2 Simulations for the viscoelastic fluid

The dimensionless parameters used in the Newtonian fluid were used in the dimensionless Oldroyd-B fluid, with the addition of We $= 0.1 - 0.5$ and $\beta = 0.59$ that were used in Chapter 5. Experimental work on the viscoelastic properties of blood was done by [84], here the properties of blood such as relaxation time and the Weissenberg number, the Wesseinburg number of normal blood was found to be between 0.1 and 0.4 for shear rates ranging near $100/s$ to $100/s$. The geometries used in the experimental work where large straight cylindrical tube, a small tube, and a porous medium. The Weissenburg numbers used in this work within range of these values and thus are applicable. The Oldroyd-B fluid presented various solution challenges. The increase in degrees of freedom from around 70000 to 280000 using the mesh in Figure 6.2 resulted in long solution times and very high memory usage, which made results untenable on a normal machine and very slow on larger machines. The significant slowdown in solver time for each iteration may stem from the use of weak boundary conditions in the constitutive relation as they apply relaxed constraints on the boundary conditions as opposed to strongly enforced boundary conditions.

To remedy this a distributed memory approach was used to parallelise the computations and the simulations were run on a 16 core machine with 64GB memory. Despite this the solution times for the viscoelastic problem were too long to run multiple cycles with dynamic code and heuristically determine a relatively cheap time step for the problem as the Oldroyd-B fluid a relatively small time step.

To obtain results ANSA was used to create a coarser yet realistic mesh. The mesh used in this case is fine enough to give an indication of the behaviour expected with varying Weissenburg numbers.

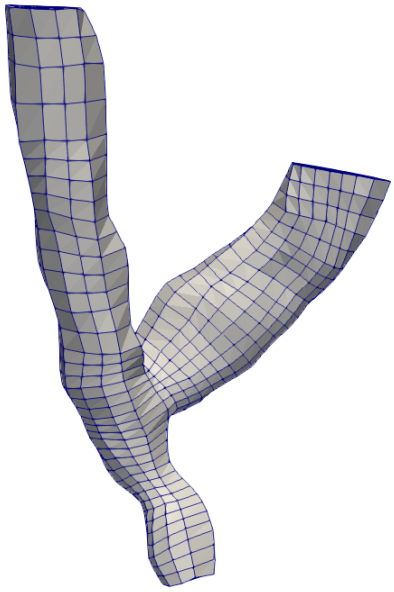

Figure 6.11: Coarse Mesh of the fistula.

Additionally piecewise discontinuous elements were used for the extra stress field, to reduce the number of degrees of freedom. The mesh in Figure 6.11 was used to obtain results for We ranging from 0.1 to 0.5, as these were the We numbers used in the benchmark test in Chapter 5.

Flow profiles

The flow profiles obtained for different We were very similar to those obtained for the Newtonian fluid. The streamlines for varying We were:

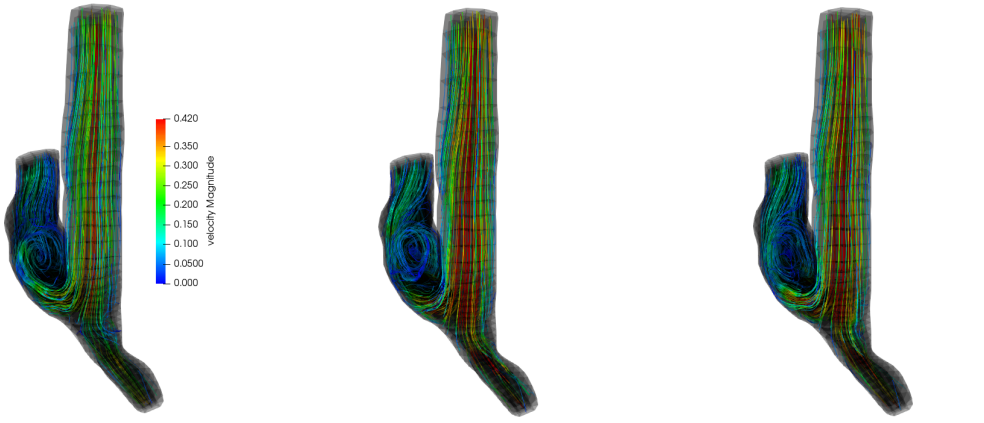

t=145ms t=345ms t=545ms

Figure 6.12: Velocity streamlines for the Oldroyd-B fluid at We = 0.1.

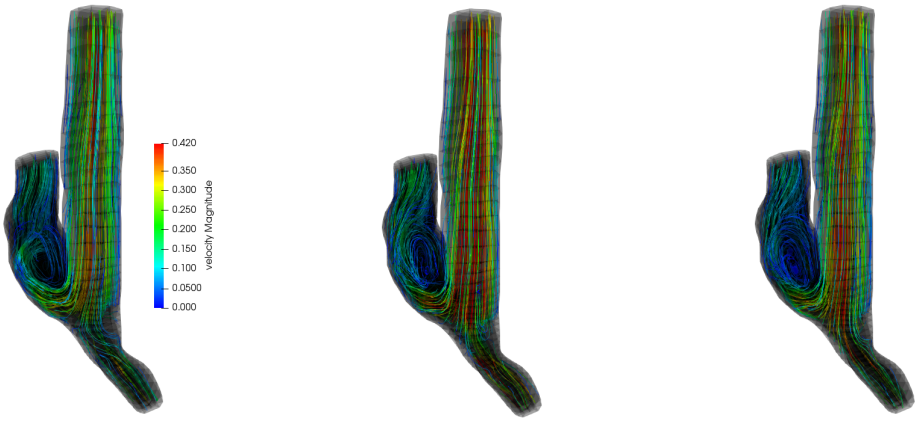

t=145ms t=345ms t=542ms

Figure 6.13: Velocity streamlines for the Oldroyd-B fluid at We = 0.2.

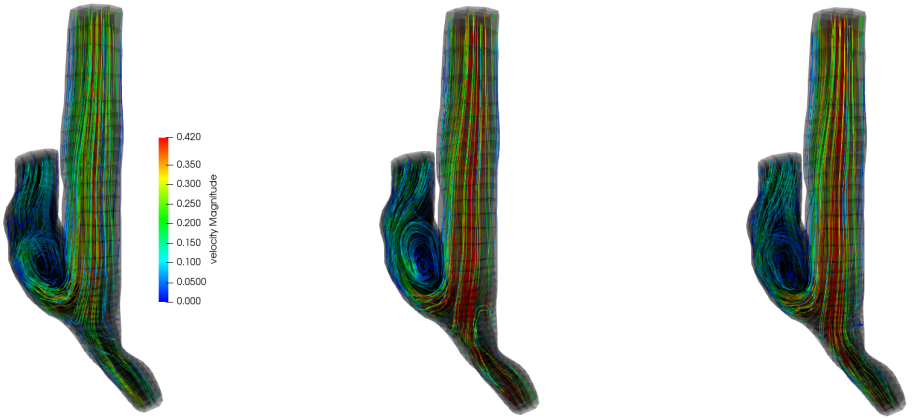

t=145ms t=345ms t=545ms

Figure 6.14: Velocity streamlines for the Oldroyd-B fluid at We = 0.3.

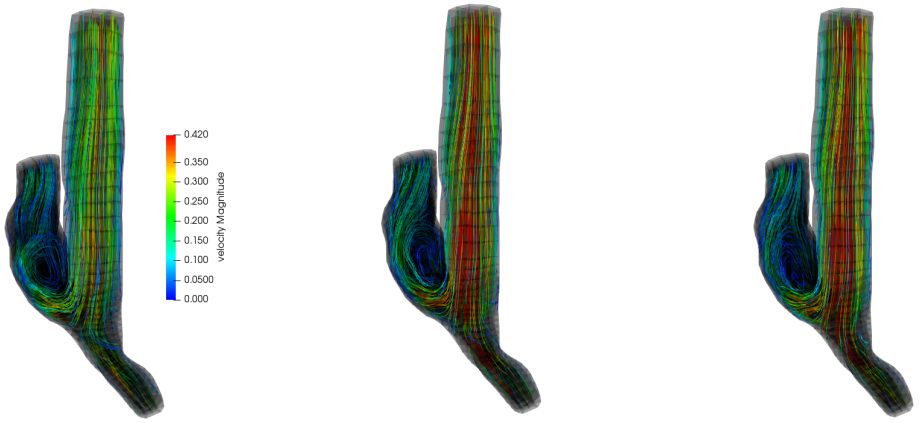

t=145ms t=345ms t=545ms

Figure 6.15: Velocity streamlines for the Oldroyd-B fluid at We = 0.4.

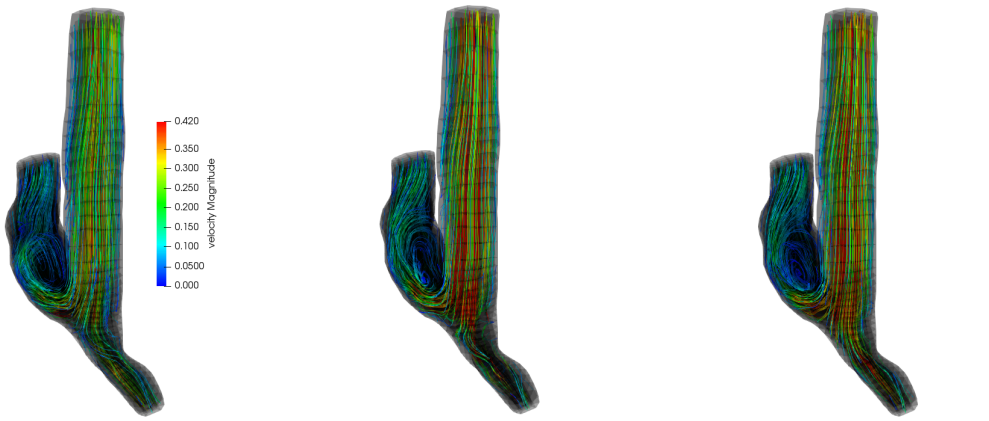

t=145ms t=345ms t=545ms

Figure 6.16: Velocity streamlines for the Oldroyd-B fluid at We = 0.5.

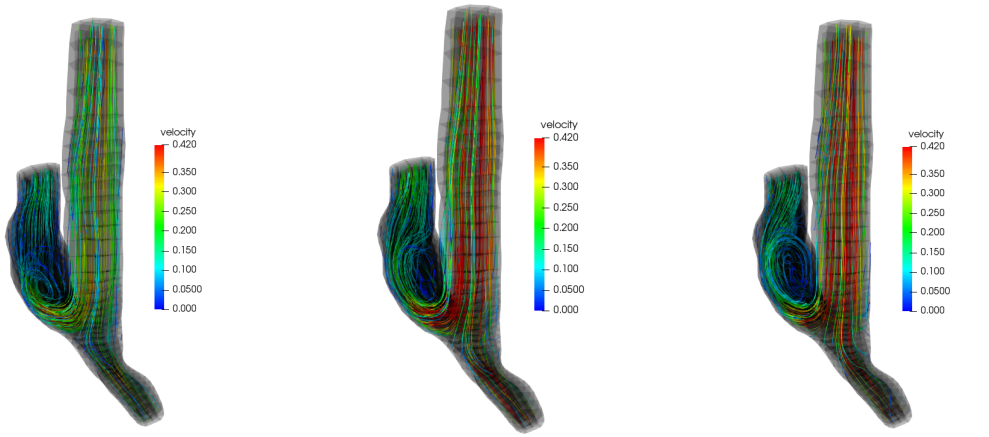

t=145ms t=345ms t=545ms

Figure 6.17: Velocity streamlines for the Newtonian fluid

The profiles were also very similar with varying We with the exception of We = 0.5, for which velocity values are lower that those obtained for other We at times greater than $445ms$.

WSS

The WSS results obtained for the Oldroyd-B fluid are compared to those for the Newtonian fluid in Figure 6.18.

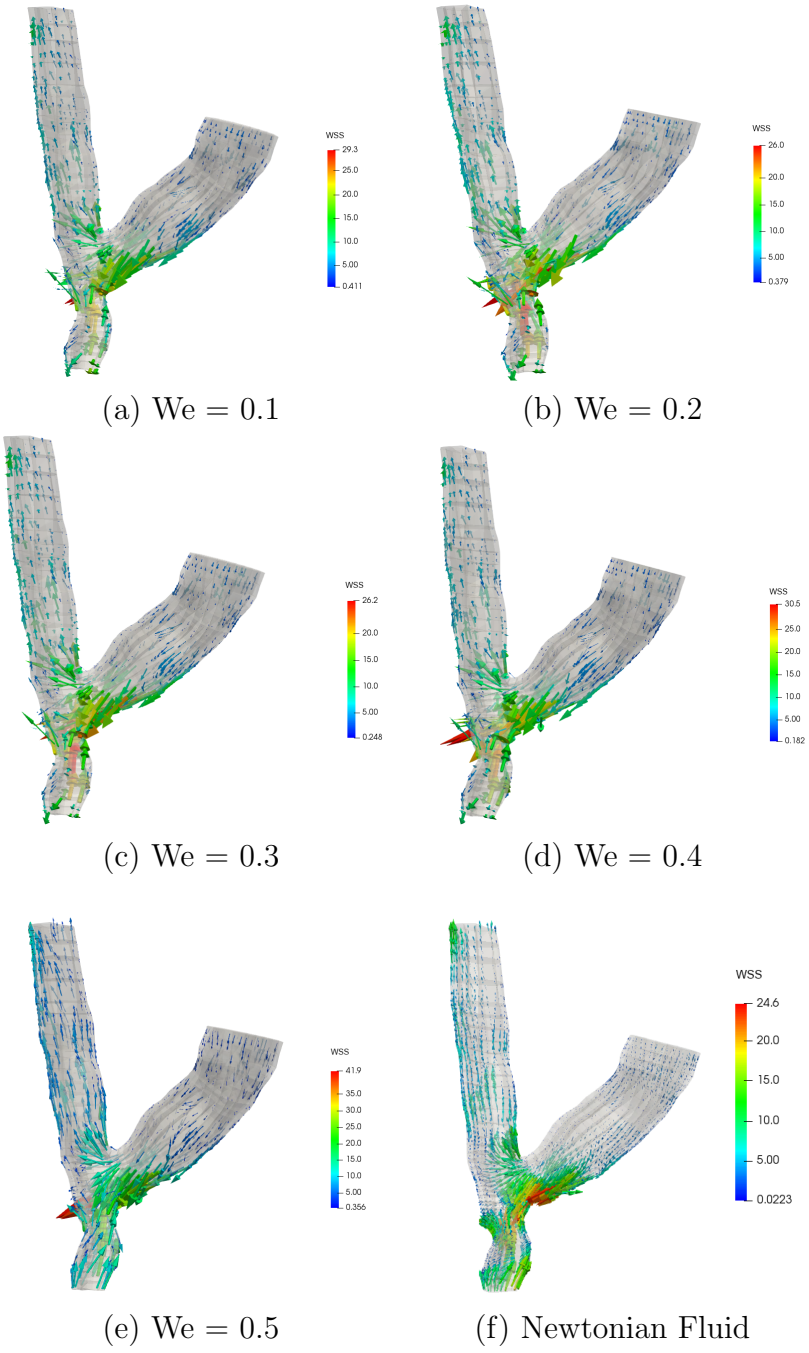

(a) We = 0.1 (b) We = 0.2

(c) We = 0.3 (d) We = 0.4

(e) We = 0.5 (f) Newtonian Fluid

Figure 6.18: WSS for varying We compared to a Newtonian fluid (f).

The direction of the WSS and the high stress regions are similar to those observed for the Newtonian fluid as shown in Figure 6.18. The coarse mesh also resulted in a relatively high stress region at the back of the junction. The maximum WSS for the Oldroyd-B fluid varies with the Weissenberg number as shown below.

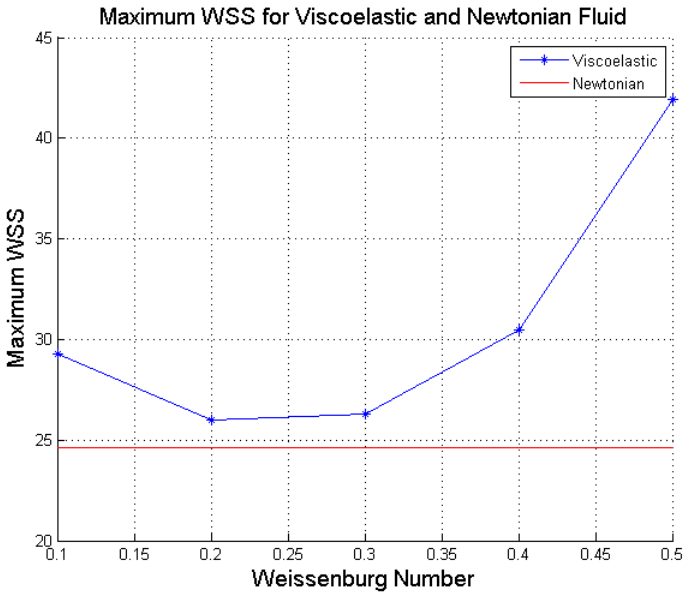

Figure 6.19: Maximum WSS for varying Weissenburg numbers.

The highest WSS occured for We = 0.5 and the variation with We is seemingly parabolic, which is similar behaviour to what was observed with the dimensionless drag in Chapter 5 and in [6, 2, 9, 42, 50]. The minimum for the WSS however has its minimum at a lower We than the dimensionless drag. The components of the extra stress were highest in the same region as the maximum WSS. The gradients of the extra stress components were found to be much steeper with increasing We.

Overall from the results obtained, the rigid wall simulations are close to those for the FSI and the MRI data in particular the flow profiles obtained are very similar. The WSS also shows the same overall trends in terms of stress direction and low stress regions, with a difference being in the base of the junction where the WSS for the rigid wall setup was closer to the maximum.

The flow profile obtained using the Oldroyd-B fluid is very similar to that obtained using a Newtonian fluid, with We = 0.5 showing a difference in velocity magnitude. The WSS obtained when using the Oldroyd-B fluid showed a different high stress region than when computed using a Newtonian fluid. In the non-Newtonian fluid higher stress were obtained at the back of the junction where as in the Newtonian fluid it is higher on the opposite side. The Newtonian fluid also exhibited higher stress than the non-Newtonian fluid at the base towards the artery outlet.

Chapter 7

Conclusions and Recommendations

The objective of this thesis was to develop a 3D finite element model of the Oldroyd-B fluid and apply it to a complex flow problem. Before addressing the 3D problem the model was verified using a 2D benchmark problem, to ensure that the correct model was implemented in the deal.ii open source libraries. The benchmark showed good results that were comparable to those in the literature with accuracy issues at higher Weissenburg numbers. The extra stress profiles and dimensionless drag obtained were very similar to the results in the literature. The result of choosing Q_1^{disc} and Q_0^{disc} elements for the extra stress showed that Q_0^{disc} under-predicted the extra stress components but was nevertheless able to capture the correct behaviour.

A 3D finite element model of a Newtonian fluid was developed with additional boundary conditions being required to obtain more realistic results for the complex geometry of the AVF. A resistance boundary condition was used to obtain realistic pressure values in the AVF. The flow profiles and WSS obtained using this model were compared to FSI results [3] and MRI data. This showed that rigid wall simulations are sufficient to obtain similar flow profiles. The WSS obtained showed that the rigid wall simulations exhibit slightly different WSS profiles. The low stress regions were very similar and the maximum WSS region was the same, with the rigid wall simulations having a lower magnitude of 29.3Pa compared to the 38Pa in the FSI simulation. The lower WSS can be attributed to the difference in the pressure boundary conditions between this work and [3], and the rigid wall not having compliance. An additional high stress region was observed in the rigid wall simulations around the base of the fistula junction.

Various computational difficulties were encountered. Firstly this problem has a considerably greater number of degrees of freedom that the Newtonian problem. As a result a challenge to obtain solutions on a standard workstation. Additionally solvers such as iterative `BCGStab` on a normal machine and parallel Trilinos solvers on a machine with 16 cores were very slow. In the end a coarser mesh was created in ANSA to obtain results

for the dynamic Oldroyd-B problem in reasonable time.

Results for the Oldroyd-B fluid were obtained for varying Weissenburg numbers. The flow profile obtained using the Oldroyd-B fluid was very similar to that seen in the Newtonian fluid, with We = 0.5 being the only one with a discernible visual difference in flow magnitude. The WSS results obtained from the Oldroyd-B fluid had a similar profile to the Newtinian fluid but with greater magnitudes for the viscoleastic fluid. The magnitude of the maximum WSS also varied quadratically with We. Similar parabolic trends can be seen in the Chapter 6, as well in the literature with the dimensionless drag [6, 2, 9, 42, 50].

From the WSS results we can see that the use of a viscoelastic fluid model for blood flow provides additional important details regarding the stresses in the AVF. Particularly that there are higher stress regions at the back of the AVF's junction when using a viscolestic fluid than in a Newtonian fluid, while lower stress in obtained near the arterial outlet when using a viscoelastic fluid. This shows that to obtain more accurate results for this particular setup one should consider the use of a viscoelatic fluid. It should be noted however that to obtain more accurate results that model the physical world using a viscoelastic would just be one of the many features that would need be considered such as considering more complex outflow boundary conditions. Since Q_0^{disc} under-predict the wall shear stresses and the use of a coarser mesh has the same result, it is expected that more accurate simulations will provide higher WSS values in the AVF. Methods for obtaining more accurate results using the Oldroyd-B fluid should be investigated; this would require a more efficient solver than that used in this work. Strongly enforced boundary conditions could also possibly remedy the solution problems by adding a different set of constraints.

In this work adaptive mesh refinement was only used in the benchmark test and not on the 3D Oldroyd-B fluid, as the mesh was too coarse to obtain any significant improvements by using adaptive refinement.This is because using adaptive refinement on a mesh this coarse would not recover the geometric curves lost when the mesh was coarsened as the original geometry cannot be used as reference to guide the refinement within the deal.ii environment. To further enhance the solutions, adaptive mesh refinement could be used however this will have to be done on a different platform other than deal.ii.
Other aspects worthy of further investigation are the use of the Windkessel boundary condition for more accurate pressures; the use of a Generalised Oldroyd-B fluid to investigate also the effect of shear rate dependence in the problem; and the comparison of WSS obtained with the uses of a range of viscoelastic models.

Bibliography

[1] I. G. Donev and B. D. Reddy, Time-dependent finite element simulations of a shear-thinning viscoelastic fluid with application to blood flow, *International Journal for Numerical Methods in Fluids*, vol. 75, no. 9, pp. 668–686, 2014.

[2] Y. Fan, R. I. Tanner, and N. Phan-Thien, Galerkin/least-square finite-element methods for steady viscoelastic flows, *Journal of Non-Newtonian Fluid Mechanics*, vol. 84, no. 2-3, pp. 233–256, 1999.

[3] A. M. de Villiers, A. T. McBride, B. D. Reddy, T. Franz, and B. S. Spottiswoode, A validated patient-specific FSI model for vascular access in haemodialysis, *Biomechanics and Modeling in Mechanobiology*, vol. 17, no. 2, pp. 479–497, 2017.

[4] T. Hayat, S. Ali Shehzad, M. Mustafa, and A. Hendi, MHD flow of an Oldroyd-B fluid through a porous channel, *International Journal of Chemical Reactor Engineering*, vol. 10, no. 1, 2012.

[5] K. K. Yeleswarapu, M. V. Kameneva, K. R. Rajagopal, and J. F. Antaki, The flow of blood in tubes: theory and experiment, *Mechanics Research Communications*, vol. 25, no. 3, pp. 257–262, 1998.

[6] I. Donev, Time dependent finite element simulations of a Generalized Oldroyd-B Fluid, Master's thesis, University of Cape Town, 11 2012.

[7] R. Keunings, On the high Weissenberg number problem, *Journal of Non-Newtonian Fluid Mechanics*, vol. 20, no. C, pp. 209–226, 1986.

[8] S. Boyaval, L. Tony, and C. Mangoubi, Free-energy-dissipative schemes for the Oldroyd-B model, *ESAIM: Mathematical Modelling and Numerical Analysis*, vol. 43, no. 3, pp. 523–561, 2009.

[9] J. M. Kim, C. Kim, K. H. Ahn, and S. J. Lee, An efficient iterative solver and high-resolution computations of the Oldroyd-B fluid flow past a confined cylinder, *Journal of Non-Newtonian Fluid Mechanics*, vol. 123, no. 2-3, pp. 161–173, 2004.

[10] J. Venkatesan and S. Ganesan, A three-field local projection stabilized formulation for computations of Oldroyd-B viscoelastic fluid flows, *Journal of Non-Newtonian Fluid Mechanics*, vol. 247, pp. 90–106, 2017.

[11] O. M. Coronado, D. Arora, M. Behr, and M. Pasquali, Four-field Galerkin/least-squares formulation for viscoelastic fluids, *Journal of Non-Newtonian Fluid Mechanics*, vol. 140, no. 1-3, pp. 132–144, 2006.

[12] Y. J. Choi, M. A. Hulsen, and H. E. H. Meijer, Simulation of the flow of a viscoelastic fluid around a stationary cylinder using an extended finite element method, *Computers and Fluids*, vol. 57, pp. 183–194, 2012.

[13] W. Guess, Fluid-structure interaction modelling of a patient-specific arteriovenous access fistula, Master's thesis, University of Cape Town, 11 2016.

[14] W. M. Lai, D. Rubin, and E. Krempl, Kinematics of a Continuum, in *Introduction to Continuum Mechanics*, pp. 69–153, 2010.

[15] R. B. Bird, R. C. Armstrong, and O. Hassager, *Dynamics of polymeric liquids. Vol. 1, 2nd Ed. : Fluid mechanics*. 1987.

[16] R. G. Owens and T. N. Phillips, *Computational rheology*. World Scientific, 2002.

[17] P. Carreau, *Rheological equations from molecular network theory*. PhD thesis, University of Wisconsin, 11 1968.

[18] H. Jeffreys, *"The Earth", 4th Edition*. Cambridge University Press, 1959.

[19] A. Robertson, a. Sequeira, and R. Owens, Rheological models for blood, *Cardiovascular Mathematics. Modeling and simulation of the circulatory system*, pp. 211–241, 2009.

[20] J. M. Dealy, Weissenberg and Deborah Numbers - Their definition and use, *Rheology Bulletin*, vol. 79, no. 2, pp. 14–18, 2010.

[21] T. J. Hughes, The Finite Element Method: Linear Static and Dynamic Finite Element Analysis, 1987.

[22] J. Fish and T. Belytschko, *A First Course in Finite Elements*. 2007.

[23] B. Reddy, *Introductory Functional Analysis: With Applications to Boundary Value Problems and Finite Elements*. Texts in Applied Mathematics, Springer New York, 2013.

[24] J. Guzman, A. Salgado, and S. Francisco-Javier, A Note on the Ladyzenskaja-Babuska-Brezzi Condition, *Arxiv preprint arXiv:1203.1870*, pp. 1–10, 2012.

[25] S. Turek, Efficient solvers for incompressible flow problems: An algorithmic and computational approach, *Computers & Mathematics with Applications*, vol. 38, no. 11-12, p. 292, 1999.

[26] W. H. Reed and T. R. Hill, Triangular Mesh Methods for the Neutron Transport Equation, *Los Alamos Report LA-UR-73-479*, no. 836, p. 10, 1973.

[27] P. Lesaint and P.-a. Raviart, On a Finite Element Method for Solving the Neutron Transport Equation, *Mathematical Aspects of Finite Elements in Partial Differential Equations*, pp. 89–145, 1974.

[28] M. Fortin and A. Fortin, A new approach for the FEM simulation of viscoelastic flows, *Journal of Non-Newtonian Fluid Mechanics*, vol. 32, no. 3, pp. 295–310, 1989.

[29] J. Donea and A. Huerta, *Finite Element Methods for Flow Problems*. 2003.

[30] M. Fortin, Old and new finite elements for incompressible flows, *International Journal for Numerical Methods in Fluids*, vol. 1, no. 4, pp. 347–364, 1981.

[31] M. Fortin and R. Pierre, On the convergence of the mixed method of Crochet and Marchal for viscoelastic flows, *Computer Methods in Applied Mechanics and Engineering*, vol. 73, no. 3, pp. 341–350, 1989.

[32] F. P. Baaijens, Mixed finite element methods for viscoelastic flow analysis: A review, *Journal of Non-Newtonian Fluid Mechanics*, vol. 79, no. 2-3, pp. 361–385, 1998.

[33] F. P. Baaijens, Application of low-order Discontinuous Galerkin methods to the analysis of viscoelastic flows, *Journal of Non-Newtonian Fluid Mechanics*, vol. 52, no. 1, pp. 37–57, 1994.

[34] P. Wriggers, *Nonlinear Finite Element Methods*. 2008.

[35] C. Paniconi and M. Putti, A comparison of Picard and Newton iteration in the numerical solution of multidimensional variably saturated flow problems, *Water Resources Research*, vol. 30, no. 12, pp. 3357–3374, 1994.

[36] P. Deuflhard, *Newton Methods for Nonlinear Problems: Affine Invariance and Adaptive Algorithms*, vol. 35. 2011.

[37] W. Bangerth, R. Hartmann, and G. Kanschat, deal.II—A general-purpose object-oriented finite element library, *ACM Transactions on Mathematical Software*, vol. 33, no. 4, pp. 24–es, 2007.

[38] D. Arndt, W. Bangerth, D. Davydov, T. Heister, L. Heltai, M. Kronbichler, M. Maier, J. P. Pelteret, B. Turcksin, and D. Wells, The deal.II library, version 8.5, 2017.

[39] W. Bangerth and O. Kayser-Herold, Data structures and requirements for hp finite element software, *ACM Transactions on Mathematical Software*, vol. 36, no. 1, pp. 1–31, 2009.

[40] A. Afonso, P. J. Oliveira, F. T. Pinho, and M. A. Alves, The log-conformation tensor approach in the finite-volume method framework, *Journal of Non-Newtonian Fluid Mechanics*, vol. 157, no. 1-2, pp. 55–65, 2009.

[41] O. M. Coronado, D. Arora, M. Behr, and M. Pasquali, A simple method for simulating general viscoelastic fluid flows with an alternate log-conformation formulation, *Journal of Non-Newtonian Fluid Mechanics*, vol. 147, no. 3, pp. 189–199, 2007.

[42] M. A. Hulsen, R. Fattal, and R. Kupferman, Flow of viscoelastic fluids past a cylinder at high Weissenberg number: Stabilized simulations using matrix logarithms, *Journal of Non-Newtonian Fluid Mechanics*, vol. 127, no. 1, pp. 27–39, 2005.

[43] K. E. Jensen, P. Szabo, and F. Okkels, Implementation of the Log-Conformation Formulation for Two-Dimensional Viscoelastic Flow, *arXiv preprint arXiv*, p. 1508.01041, 2015.

[44] P. Knechtges, M. Behr, and S. Elgeti, Fully-implicit log-conformation formulation of constitutive laws, *Journal of Non-Newtonian Fluid Mechanics*, vol. 214, pp. 78–87, 2014.

[45] M. G. Baltussen, Y. J. Choi, M. A. Hulsen, and P. D. Anderson, Weakly-imposed Dirichlet boundary conditions for non-Newtonian fluid flow, *Journal of Non-Newtonian Fluid Mechanics*, vol. 166, no. 17-18, pp. 993–1003, 2011.

[46] M. Alves, F. Pinho, and P. Oliveira, The flow of viscoelastic fluids past a cylinder: finite-volume high-resolution methods, *Journal of Non-Newtonian Fluid Mechanics*, vol. 97, pp. 207–232, 2001.

[47] H. S. Dou and N. Phan-Thien, The flow of an Oldroyd-B fluid past a cylinder in a channel: adaptive viscosity vorticity (DAVSS-??) formulation, *Journal of Non-Newtonian Fluid Mechanics*, vol. 87, no. 1, pp. 47–73, 1999.

[48] M. Sahin and H. J. Wilson, A semi-staggered dilation-free finite volume method for the numerical solution of viscoelastic fluid flows on all-hexahedral elements, *Journal of Non-Newtonian Fluid Mechanics*, vol. 147, no. 1-2, pp. 79–91, 2007.

[49] R. M. Kynch and T. N. Phillips, A high resolution spectral element approximation of viscoelastic flows in axisymmetric geometries using a DEVSS-G/DG formulation, *Journal of Non-Newtonian Fluid Mechanics*, vol. 240, pp. 15–33, 2017.

[50] S. Claus and T. N. Phillips, Viscoelastic flow around a confined cylinder using spectral/hp element methods, *Journal of Non-Newtonian Fluid Mechanics*, vol. 200, pp. 131–146, 2013.

[51] R. G. Owens, C. Chauvière, and T. N. Philips, A locally-upwinded spectral technique (LUST) for viscoelastic flows, *Journal of Non-Newtonian Fluid Mechanics*, vol. 108, no. 1-3, pp. 49–71, 2002.

[52] A. Vázquez-Quesada and M. Ellero, SPH simulations of a viscoelastic flow around a periodic array of cylinders confined in a channel, *Journal of Non-Newtonian Fluid Mechanics*, vol. 167-168, pp. 1–8, 2012.

[53] Y. L. Xiong, C. H. Bruneau, and H. Kellay, Flow past a cylinder in diluted polymer solutions, *Journal of Physics: Conference Series*, vol. 318, no. 9, p. 092021, 2011.

[54] J. M. Verhelst and F. T. M. Nieuwstadt, Visco-elastic flow past circular cylinders mounted in a channel: Experimental measurements of velocity and drag, *Journal of Non-Newtonian Fluid Mechanics*, vol. 116, no. 2-3, pp. 301–328, 2004.

[55] S. Chien, S. Usami, R. J. Dellenback, M. I. Gregersen, L. B. Nanninga, and M. M. Guest, Blood viscosity: influence of erythrocyte aggregation., *Science (New York, N.Y.)*, vol. 157, no. 3790, pp. 829–31, 1967.

[56] L. Formaggia, A. Quarteroni, and A. Veneziani, *Cardiovascular Mathematics: Modeling and simulation of the circulatory system.* 2009.

[57] D. F. Young and F. Y. Tsai, Flow characteristics in models of arterial stenoses - II. Unsteady flow, *Journal of Biomechanics*, vol. 6, no. 5, pp. 547–559, 1973.

[58] T. Bodnár, A. Sequeira, and M. Prosi, On the shear-thinning and viscoelastic effects of blood flow under various flow rates, in *Applied Mathematics and Computation*, vol. 217, pp. 5055–5067, 2011.

[59] a. Leuprecht and K. Perktold, Computer simulation of non-newtonian effects on blood flow in large arteries., *Computer methods in biomechanics and biomedical engineering*, vol. 4, no. 2, pp. 149–163, 2001.

[60] G. Pontrelli, Blood flow through an axisymmetric stenosis, *Proceedings of the Institution of Mechanical Engineers, Part H: Journal of Engineering in Medicine*, vol. 215, no. 1, pp. 1–10, 2001.

[61] L. Nadau and A. Sequeira, Numerical simulations of shear dependent viscoelastic flows with a combined finite element-finite volume method, *Computers and Mathematics with Applications*, vol. 53, no. 3-4, pp. 547–568, 2007.

[62] C. Tu and M. Deville, Pulsatile flow of Non-Newtonian fluids through arterial stenoses, *Journal of Biomechanics*, vol. 29, no. 7, pp. 899–908, 1996.

[63] I. E. Vignon-Clementel, C. Alberto Figueroa, K. E. Jansen, and C. A. Taylor, Outflow boundary conditions for three-dimensional finite element modeling of blood flow and pressure in arteries, *Computer Methods in Applied Mechanics and Engineering*, vol. 195, no. 29-32, pp. 3776–3796, 2006.

[64] I. Vignon-Clementel, C. Figueroa, K. Jansen, and C. Taylor, Outflow boundary conditions for 3D simulations of non-periodic blood flow and pressure fields in deformable arteries, *Computer Methods in Biomechanics and Biomedical Engineering*, vol. 13, no. 5, pp. 625–640, 2010.

[65] I. Decorato, Z. Kharboutly, T. Vassallo, J. Penrose, C. Legallais, and A. V. Salsac, Numerical simulation of the fluid structure interactions in a compliant patient-specific arteriovenous fistula, *International Journal for Numerical Methods in Biomedical Engineering*, vol. 30, no. 2, pp. 143–159, 2014.

[66] G. Pontrelli, Blood flow through a circular pipe with an impulsive pressure gradient, *Mathematical Models and Methods in Applied Sciences*, vol. 10, no. 2, 2000.

[67] M. Hulsen, A. van Heel, and B. van den Brule, Simulation of viscoelastic flows using Brownian configuration fields, *Journal of Non-Newtonian Fluid Mechanics*, vol. 70, no. 1-2, pp. 79–101, 1997.

[68] M. Anand and K. R. Rajagopal, A shear-thinning viscoelastic fluid model for describing the flow of blood, *International Journal of Cardiovascular Medicine and Science*, vol. 4, no. 2, pp. 59–68, 2004.

[69] G. B. Thurston, Viscoelasticity of Human Blood, *Biophysical Journal*, vol. 12, no. 9, pp. 1205–1217, 1972.

[70] K. D. Smith and A. Sequeira, Micro-macro simulations of a shear-thinning viscoelastic kinetic model: Applications to blood flow, *Applicable Analysis*, vol. 90, no. 1, pp. 227–252, 2011.

[71] I. Decorato, Z. Kharboutly, C. Legallais, and A. V. Salsac, Numerical study of the influence of wall compliance on the haemodynamics in a patient-specific arteriovenous fistula, *Computer Methods in Biomechanics and Biomedical Engineering*, vol. 14, no. SUPPL.1, pp. 121–123, 2011.

[72] S. W. Lee, D. S. Smith, F. Loth, P. F. Fischer, and H. S. Bassiouny, Importance of flow division on transition to turbulence within an arteriovenous graft, *Journal of Biomechanics*, vol. 40, no. 5, pp. 981–992, 2007.

[73] I. Van Tricht, D. De Wachter, J. Tordoir, and P. Verdonck, Hemodynamics and complications encountered with arteriovenous fistulas and grafts as vascular access for hemodialysis: A review, in *Annals of Biomedical Engineering*, vol. 33, pp. 1142–1157, 2005.

[74] M. Boghosian, K. Cassel, M. Hammes, B. Funaki, S. Kim, X. Qian, X. Wang, P. Dhar, and J. Hines, Hemodynamics in the cephalic arch of a brachiocephalic fistula, *Medical Engineering and Physics*, vol. 36, no. 7, pp. 822–830, 2014.

[75] L. Botti, K. Van Canneyt, R. Kaminsky, T. Claessens, R. N. Planken, P. Verdonck, A. Remuzzi, and L. Antiga, Numerical Evaluation and Experimental Validation of Pressure Drops Across a Patient-Specific Model of Vascular Access for Hemodialysis, *Cardiovascular Engineering and Technology*, vol. 4, no. 4, pp. 485–499, 2013.

[76] K. Van Canneyt, T. Pourchez, S. Eloot, C. Guillame, A. Bonnet, P. Segers, and P. Verdonck, Hemodynamic impact of anastomosis size and angle in side-to-end arteriovenous fistulae: A computer analysis, *Journal of Vascular Access*, vol. 11, no. 1, pp. 52–58, 2010.

[77] A. K. Niemann, J. Udesen, S. Thrysoe, J. V. Nygaard, E. T. Fründ, S. E. Petersen, and J. M. Hasenkam, Can sites prone to flow induced vascular complications in a-v fistulas be assessed using computational fluid dynamics?, *Journal of Biomechanics*, vol. 43, no. 10, pp. 2002–2009, 2010.

[78] B. Ene-Iordache and A. Remuzzi, Disturbed flow in radial-cephalic arteriovenous fistulae for haemodialysis: Low and oscillating shear stress locates the sites of stenosis, *Nephrology Dialysis Transplantation*, vol. 27, no. 1, pp. 358–368, 2012.

[79] H. S. Ryou, S. Kim, and K. Ro, A numerical study of the effect of catheter angle on the blood flow characteristics in a graft during hemodialysis, *Korea Australia Rheology Journal*, vol. 25, no. 1, pp. 19–27, 2013.

[80] P. M. McGah, D. F. Leotta, K. W. Beach, and A. Aliseda, Effects of wall distensibility in hemodynamic simulations of an arteriovenous fistula, *Biomechanics and Modeling in Mechanobiology*, vol. 13, no. 3, pp. 679–695, 2014.

[81] M. Esmaily Moghadam, Y. Bazilevs, T. Y. Hsia, I. E. Vignon-Clementel, and A. L. Marsden, A comparison of outlet boundary treatments for prevention of backflow divergence with relevance to blood flow simulations, *Computational Mechanics*, vol. 48, no. 3, pp. 277–291, 2011.

[82] Y. Bazilevs, J. R. Gohean, T. J. R. Hughes, R. D. Moser, and Y. Zhang, Patient-specific isogeometric fluid-structure interaction analysis of thoracic aortic blood flow

due to implantation of the Jarvik 2000 left ventricular assist device, *Computer Methods in Applied Mechanics and Engineering*, vol. 198, no. 45-46, pp. 3534–3550, 2009.

[83] I. Vignon, *A coupled multidomain method for computational modeling of blood flow*. PhD thesis, Stanford University, 11 2006.

[84] G. B. Thurston and N. M. Henderson, Effects of flow geometry on blood viscoelasticity., *Biorheology*, vol. 43 6, pp. 729–46, 2006.